

How to build a water-splitting machine: structural insights into photosystem II assembly

Jure Zabret

Ruhr University Bochum

Stefan Bohn

Max Planck Institute of Biochemistry

Sandra Schuller

Max Planck Institute of Biochemistry

Oliver Arnolds

Ruhr University Bochum <https://orcid.org/0000-0003-1433-1233>

Madeline Möller

Ruhr University Bochum

Jakob Meier-Credo

Max Planck Institute of Biophysics

Pasqual Liauw

Ruhr University Bochum

Aaron Chan

University of Illinois at Urbana-Champaign

Emad Tajkhorshid

University of Illinois at Urbana-Champaign

Julian Langer

Max Planck Institute of Biophysics

Raphael Stoll

Ruhr University Bochum

Anja Krieger-Liszkay

Université Paris-Saclay

Benjamin Engel

Helmholtz Zentrum München

Till Rudack

Ruhr University Bochum

Jan Schuller

Phillips University Marburg <https://orcid.org/0000-0002-9121-1764>

Marc Nowaczyk (✉ Marc.M.Nowaczyk@rub.de)

Ruhr University Bochum <https://orcid.org/0000-0002-9269-0672>

Article

Keywords: photosynthesis, photosystem II biogenesis, assembly factors, bicarbonate binding, reactive 15 oxygen species, protection mechanisms, oxygen evolving complex, photoactivation, cryo-EM

Posted Date: October 23rd, 2020

DOI: <https://doi.org/10.21203/rs.3.rs-88039/v1>

License:   This work is licensed under a Creative Commons Attribution 4.0 International License.

[Read Full License](#)

Version of Record: A version of this preprint was published at Nature Plants on April 12th, 2021. See the published version at <https://doi.org/10.1038/s41477-021-00895-0>.

How to build a water-splitting machine: structural insights into photosystem II assembly

Jure Zabret^{1#}, Stefan Bohn^{2#}, Sandra K. Schuller^{3,4}, Oliver Arnolds⁵, Madeline Möller¹, Jakob Meier-Credo⁶, Pasqual Liauw¹, Aaron Chan⁷, Emad Tajkhorshid⁷, Julian D. Langer^{6,8}, Raphael Stoll⁵, Anja Krieger-Liszkay⁹, Benjamin D. Engel^{2,10,11}, Till Rudack^{12,13,*}, Jan M. Schuller^{3,4,*}, Marc M. Nowaczyk^{1,*}

Affiliations:

¹Department of Plant Biochemistry, Faculty of Biology & Biotechnology, Ruhr University Bochum, 44780 Bochum, Germany.

²Department of Molecular Structural Biology, Max Planck Institute of Biochemistry, 82152 Martinsried, Germany.

³Department of Structural Cell Biology, Max Planck Institute of Biochemistry, 82152 Martinsried, Germany.

⁴SYNMIKRO Research Center, Philipps-University Marburg, 35043 Marburg, Germany.

⁵Biomolecular Spectroscopy and RUBiospek|NMR, Faculty of Chemistry and Biochemistry, Ruhr-University Bochum, 44780 Bochum, Germany

⁶Department of Molecular Membrane Biology, Max Planck Institute of Biophysics, 60438 Frankfurt/Main, Germany.

⁷NIH Center for Macromolecular Modeling and Bioinformatics, Beckman Institute for Advanced Science and Technology, Department of Biochemistry, and Center for Biophysics and Quantitative Biology, University of Illinois at Urbana-Champaign, Urbana, Illinois

⁸Max Planck Institute for Brain Research, Max von Laue Strasse 4, 60438 Frankfurt/Main, Germany.

⁹Université Paris-Saclay, CEA, CNRS, Institute for Integrative Biology of the Cell (I2BC), 91198, Gif-sur-Yvette, France

¹⁰Helmholtz Pioneer Campus, Helmholtz Zentrum München, Ingolstädter Landstraße 1, 85764 Neuherberg, Germany.

¹¹Department of Chemistry, Technical University of Munich, Lichtenbergstraße 4, 85748 Garching, Germany.

¹²Biospectroscopy, Center for Protein Diagnostics (ProDi), Ruhr University Bochum, 44801 Bochum, Germany.

¹³Department of Biophysics, Faculty of Biology & Biotechnology, Ruhr University Bochum, 44780 Bochum, Germany.

#Equal contribution

*corresponding authors: till.rudack@rub.de, jan.schuller@synmikro.uni-marburg.de, marc.m.nowaczyk@rub.de

One Sentence Highlight:

The high-resolution Cryo-EM structure of the photosystem II assembly intermediate PSII-I reveals how nature's water splitting catalyst is assembled, protected and prepared for photoactivation by help of the three assembly factors Psb27, Psb28 and Psb34.

1 **Abstract**

2 Biogenesis of photosystem II (PSII), nature's water splitting catalyst, is assisted by auxiliary
3 proteins that form transient complexes with PSII components to facilitate stepwise assembly
4 events. Using cryo-electron microscopy, we solved the structure of such a PSII assembly
5 intermediate with 2.94 Å resolution. It contains three assembly factors (Psb27, Psb28, Psb34)
6 and provides detailed insights into their molecular function. Binding of Psb28 induces large
7 conformational changes at the PSII acceptor side, which distort the binding pocket of the mobile
8 quinone (Q_B) and replace bicarbonate with glutamate as a ligand of the non-heme iron, a
9 structural motif found in reaction centers of non-oxygenic photosynthetic bacteria. These
10 results reveal novel mechanisms that protect PSII from damage during biogenesis until water
11 splitting is activated. Our structure further demonstrates how the PSII active site is prepared for
12 the incorporation of the Mn₄CaO₅ cluster, which performs the unique water splitting reaction.

13 **Keywords**

14 photosynthesis, photosystem II biogenesis, assembly factors, bicarbonate binding, reactive
15 oxygen species, protection mechanisms, oxygen evolving complex, photoactivation, cryo-EM

16 **Introduction**

17 Photosystem II (PSII) is the only enzyme that catalyzes the light-driven oxidation of water, a
18 thermodynamically demanding reaction that drives photosynthesis, sustaining life on our
19 planet¹⁻³. This multi-subunit membrane protein complex is located in the thylakoid membranes
20 of cyanobacteria, algae and plants. PSII strips electrons from water and injects them into the
21 photosynthetic electron transport chain (PET). It forms a homodimer with a molecular mass of
22 ~500 kDa⁴, with each monomer composed of at least 20 protein subunits and numerous
23 cofactors, including chlorophylls, quinones, carotenoids, lipids, bicarbonate and the unique
24 Mn₄CaO₅ cluster⁵⁻⁷. The two core proteins D1 and D2 form a central, membrane-intrinsic
25 heterodimer, which binds all important redox cofactors involved in internal electron transfer⁸.
26 Light-excitation leads to a charge-separated state in which an electron is transferred from the
27 chlorophyll assembly P₆₈₀⁹ to the nearby pheophytin¹⁰. Subsequently, the electron is passed to
28 the bound plastoquinone (Q_A) and then to the mobile plastoquinone molecule (Q_B), which
29 leaves the complex after accepting two electrons and two protons¹¹. The electron hole at P₆₈₀ is
30 filled by oxidation of an adjacent tyrosine residue (Tyr_Z)¹² and finally by the oxygen evolving

31 complex (OEC) that contains the Mn_4CaO_5 cluster. In cyanobacteria, the cluster is shielded at
32 the luminal side by the three extrinsic proteins, PsbO, PsbU and PsbV, which regulate access
33 to the OEC by forming a complex network of channels for different substrates and products¹³.
34 Light energy is collected and funneled towards P_{680} by the two membrane-intrinsic antenna
35 proteins CP43 and CP47. These proteins bind most of the chlorophyll molecules and are located
36 at opposite sides of the D1/D2 heterodimer¹⁴. Moreover, at least twelve small transmembrane
37 subunits with one or two transmembrane helices have been identified in PSII¹⁵, including
38 cytochrome- b_{559} ¹⁶.

39 Structural and spectroscopic investigations have revealed these aforementioned comprehensive
40 insights into PSII function¹⁷⁻²¹, but we are far from understanding PSII biogenesis with
41 molecular detail. How nature facilitates the assembly of a multi-subunit, multi-cofactor
42 membrane protein complex is a fundamental unsolved question. The biogenesis of PSII is even
43 more challenging, as the mature complex performs sophisticated and extreme redox chemistry
44 to catalyze the light-driven oxidation of water. This can easily lead to the formation of reactive
45 oxygen species (e.g., singlet oxygen is produced by triplet chlorophyll in the PSII reaction
46 center) and subsequent loss of function due to damaged proteins and cofactors^{22,23}. Biogenesis
47 intermediates with only partially functional fragments of the redox chain are particularly prone
48 to damage, thus demanding specialized protection mechanisms for the assembly process.
49 Therefore, PSII biogenesis is not a spontaneous process but rather must be tightly regulated by
50 the action of assembly factors. Thus far, more than 20 auxiliary proteins have been identified
51 that guide the stepwise assembly of PSII subunits and cofactors via intermediate modules,
52 which are assembled independently and then joined together to produce mature PSII²⁴⁻²⁶. In
53 cyanobacteria, PSII biogenesis begins with the formation of the D1/D2 heterodimer reaction
54 center (RC) complex from the D1 precursor protein (pD1) and the D2 protein. This is assisted
55 by the PSII assembly factor Ycf48 after partial processing of the D1 C-terminal extension by
56 the D1 specific peptidase CtpA^{27,28}. In the next step, the assembly factor Psb28 helps CP47 join
57 the RC complex to form the RC47 complex, in which iD1 is further processed to its mature
58 form by CtpA^{29,30}. Almost all ligands of the Mn_4CaO_5 cluster are already present at this stage,
59 except for those provided by CP43, which comes pre-constructed with assembly factor Psb27
60 and several small subunits (together called the CP43 module)³¹. Psb28 is released as CP43
61 binds, and the resulting Psb27-PSII monomer is activated by maturation of the OEC and the
62 binding of the extrinsic proteins PsbO, PsbU and PsbV³²⁻³⁴. Finally, PSII biogenesis completes
63 with dimerization of two fully assembled monomers and attachment of the soluble
64 phycobilisome antenna complexes. Interestingly, deletion of *psbJ*, which encodes a small single

65 transmembrane helix protein at the entrance of the PSII plastoquinone channel, leads to massive
66 accumulation of an intermediate monomeric PSII complex, which contains both assembly
67 factors Psb27 and Psb28³⁵.

68 Physiological studies of Psb27 and Psb28 deletion strains point towards multifaceted functions.
69 Cyanobacterial mutants lacking Psb28 exhibited slower autotrophic growth, particularly under
70 stress conditions^{30,36}, and limited synthesis of Chl-binding proteins but without decrease in PSII
71 functionality³⁰. The Psb28 mutant also exhibited an overall increase in PSII repair and faster
72 recovery from photodamage³⁰. Chemical cross-linking combined with mass spectrometry
73 revealed that Psb28 binds to the cytosolic side of CP47 close to cytochrome-b₅₅₉ and the
74 Q_B binding site. Based on this, researchers postulated a protective role for Psb28, whereby it
75 blocks electron transport to the acceptor side of PSII, thereby protecting the RC47 complex
76 from excess photodamage during the assembly process³⁷. This hypothesis is strengthened by
77 the observation that Psb28 is also found in PSII repair complexes³⁸. The luminal PSII assembly
78 factor Psb27 has been similarly well investigated. This lipoprotein is predominantly associated
79 with inactive PSII fractions involved in assembly or repair^{31,33,38-42} stabilizing the CP43 luminal
80 domain and presumably facilitating the assembly of the OEC.

81 Our current knowledge of PSII biogenesis mainly describes the order of events and protein
82 composition of each intermediate, as well as the general roles of PSII assembly factors.
83 However, the precise molecular functions of these intermediate complexes and the involved
84 assembly factors are still elusive due to their low abundance and intrinsic instability. High-
85 resolution structural information is of vital importance to gain a deeper understanding into the
86 molecular action of PSII assembly factors, as they are proposed to alter the structures of their
87 associated PSII proteins to provide protection or facilitate specific biogenesis transitions.

88 Here, we use cryo-EM single particle analysis to describe the first molecular structure of a PSII
89 assembly intermediate. This structure represents one of the key transitions in PSII biogenesis:
90 the attachment of the CP43 module to the pre-assembled RC47 reaction center complex, which
91 precedes incorporation and activation of the Mn₄CaO₅ cluster. We complement this structural
92 data with spectroscopic analysis, revealing the first detailed insights into the molecular
93 mechanisms of PSII assembly. Our study provides mechanistic answers to three long-standing
94 questions: i) How do assembly factors modulate the structures of PSII subunits to assist
95 biogenesis? ii) How is PSII protected from photodamage during assembly? iii) How is the PSII
96 active site prepared for incorporation of the Mn₄CaO₅ cluster?

97 **Results**

98 **Structure determination of the PSII assembly intermediate (PSI-I)**

99 Stable PSII intermediates were purified from the *T. elongatus* $\Delta psbJ$ mutant³⁵ by affinity
100 chromatography using a twin-strep-tag fused to the C-terminus of the CP43 subunit and
101 subsequent ion exchange chromatography (Fig. S1A). The main peak of the IEC profile
102 corresponds primarily to monomeric PSII, which lacks the extrinsic subunits PsbO, PsbU and
103 PsbV that are indicative for water splitting activity (Fig. S1B and C). Single particle cryo-EM
104 analysis of this PSII fraction resulted in three different high-resolution maps that allowed model
105 building with high confidence and excellent statistics (Fig. S2, Table S1). In addition to the
106 protein subunits, we also faithfully assigned all essential non-protein cofactors, including
107 chlorophylls, quinones, carotenoids and lipids, which are also present in the mature PSII
108 complex (Fig. S3). Consistent with previous biochemical studies^{33,35,40}, the EM density
109 corresponding to the fully assembled, active Mn_4CaO_5 cluster is missing in the purified
110 biogenesis intermediates. The first cryo-EM map (2.94 Å), which we call PSII-I (for PSII-
111 Intermediate), provides a snapshot of the attachment of the CP43 module to the pre-assembled
112 RC47 reaction center complex (Fig. 1). This PSII intermediate contains three assembly factors
113 (Psb27, Psb28 and Psb34), as well as almost all the membrane-intrinsic subunits and cofactors
114 found in mature PSII. Psb27 and Psb28 are well-known assembly factors^{30,31,34,35,43}, whereas
115 the additional single transmembrane helix protein (tsl0063), which we named Psb34, has not
116 been described before. The small subunit PsbY, which is known to be loosely bound⁴⁴, is not
117 resolved in our structure. In addition, PsbJ is not present, as the corresponding gene was
118 inactivated to stall PSII assembly at this specific transition³⁵.

119 The two additional maps serve as internal controls. PSII-I' (2.76 Å) lacks Psb27 but is otherwise
120 comparable to PSII-I; the root mean square deviation (RMSD) of the C_α atomic positions
121 between similar subunits of the two complexes is 0.4 Å. Most likely, Psb27 was partly lost
122 during sample preparation. The third cryo-EM map (2.82 Å), which we call PSII-M (for PSII-
123 Monomer), represents a monomeric PSII complex without bound assembly factors.
124 Comparison of our PSII-M structure with a crystal structure of monomeric PSII⁴⁴ (PDB-ID
125 3KZI, 3.6 Å) reveals only minimal differences between both structures, with a C_α RMSD of
126 1.3 Å, which verifies that the structural changes observed in PSII-I are not caused by the
127 deletion of PsbJ.

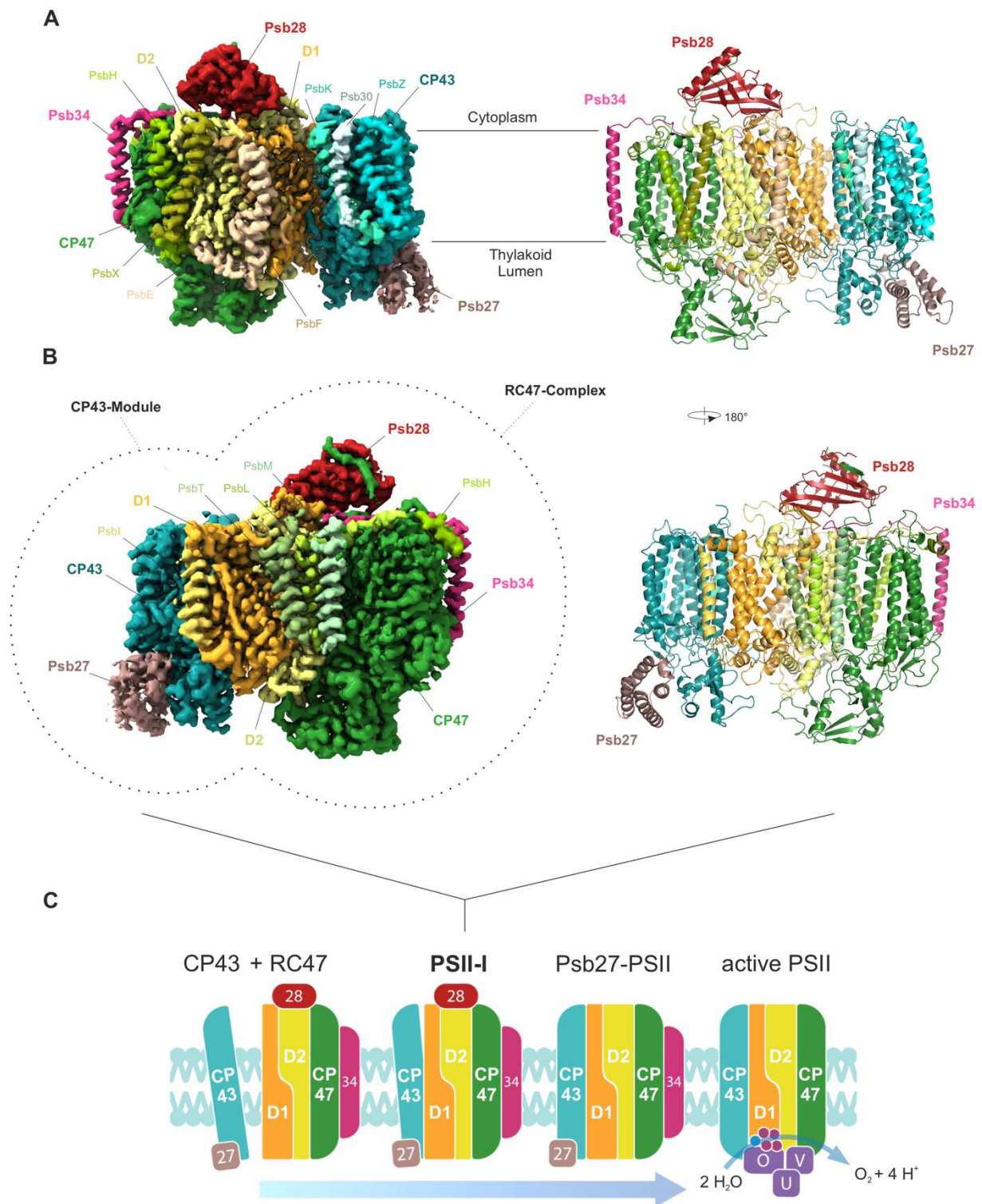


Fig. 1: Cryo-EM map of a PSII assembly intermediate (PSII-I) from *T. elongatus*, segmented by subunit. (A) 15 PSII subunits and 3 assembly factors are colored and named (PSII subunits: D1, D2, CP43, CP47, PsbE, PsbF, PsbH, PsbI, PsbK, PsbL, PsbM, PsbT, PsbX, PsbZ and Psb30; assembly factors: Psb27, Psb28 and *tsl0063*, which we named Psb34) (front view). (B) Parts of PSII that originate from the CP43 module (comprised of CP43, Psb27, PsbZ, Psb30 and PsbK) and the RC47 complex are indicated by dashed lines (back view). Schematic model of the PSII assembly process starting with the formation of PSII-I from the CP43 module and RC47. Small PSII subunits were omitted for simplicity.

128 **Psb34 specifically assists the attachment of the CP43 module to RC47**

129 Our PSII-I structure provides the first identification of the single transmembrane helix protein
130 Psb34 bound to a PSII assembly intermediate (Fig. 2A), which we also confirmed by mass
131 spectrometry (Fig. 2B). Psb34 was probably overlooked previously due to its hydrophobicity
132 and small size. It has a single transmembrane helix that binds to the CP47 antenna protein in
133 close proximity to PsbH (Fig. 2A). Its conserved long N-terminal arm is located at the side and
134 top of the D2 subunit (Fig. 2A). In addition, we independently confirmed the interaction of
135 Psb34 with PSII assembly intermediates by isolation of strep-tagged Psb34 complexes,
136 indicating a specific function of Psb34 in the attachment of CP43 to RC47 (Fig. 2C). Two
137 distinct PSII intermediates were isolated via pulldown of strep-tagged Psb34: the RC47
138 complex with bound Psb28 and the subsequent PSII intermediate after attachment of CP43 and
139 Psb27 (Fig. 2C). This observation implies that Psb28 is usually released from the PSII
140 intermediate after attachment of CP43, probably after incorporation of PsbJ, as this trigger is
141 missing in the analyzed $\Delta psbJ$ mutant. Psb34 shows sequence similarity to high-light inducible
142 proteins (HLIPs), which play a role in transient chlorophyll storage and chlorophyll
143 biosynthesis⁴⁵. However, the chlorophyll binding motive is missing in Psb34 (Table S2),
144 suggesting a distinct function for this protein in PSII biogenesis.

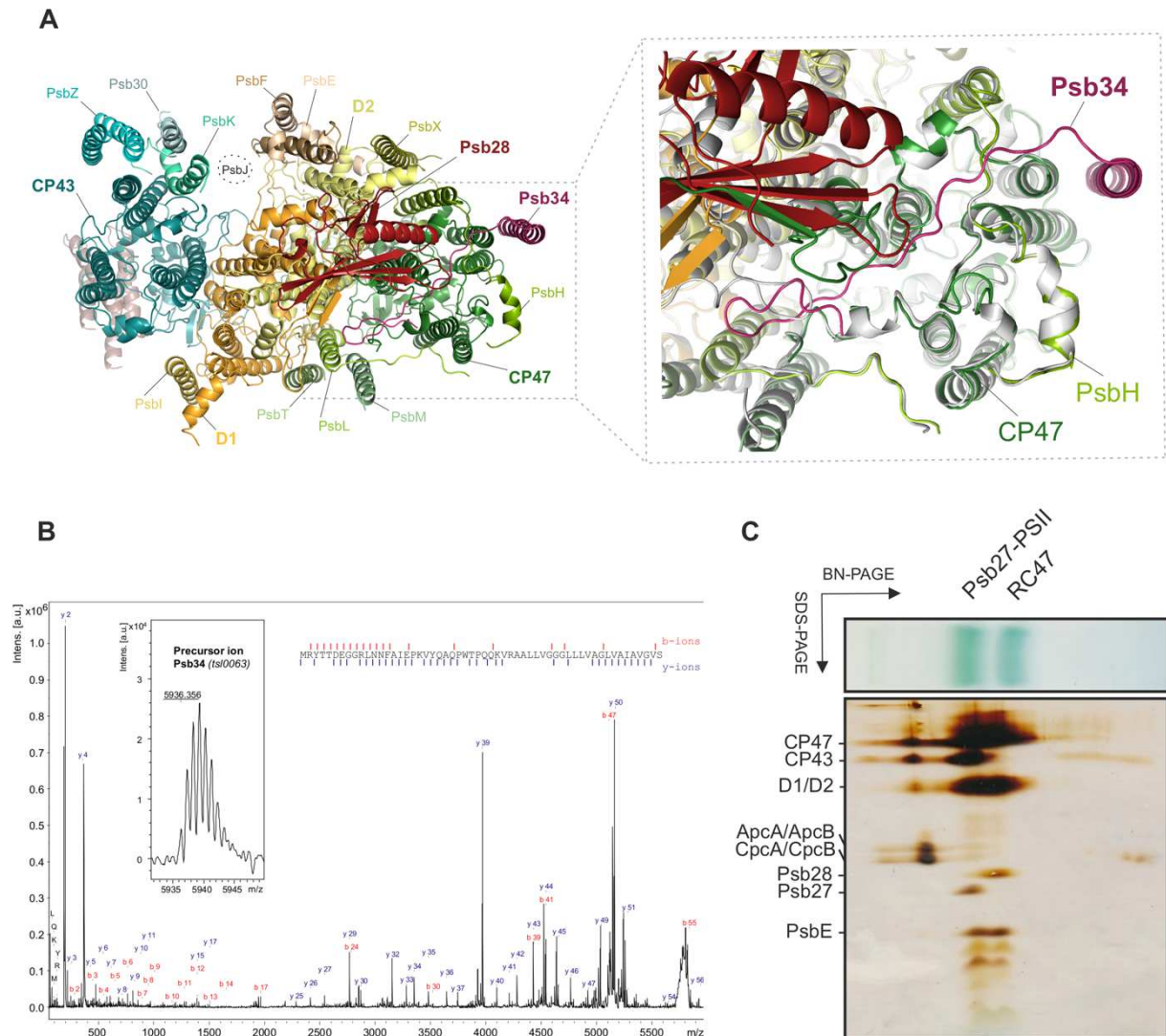


Fig. 2: **Psb34 binds to RC47 during attachment of the CP43 module.** (A) Binding site of Psb34 at CP47, close to PsbH (top view), with extended binding of the Psb34 N-terminus along the cytoplasmic PSII surface (dashed box). (B) MALDI-ToF analysis of PSII assembly intermediates. Mass spectrum of Psb34 (tsl0063) from the PSII complex (inset) and the fragment spectrum obtained for m/z 5936.356 with annotated b- and y-ion series matching the Psb34 sequence. Observed fragmentation sites are indicated by dashes in the sequence. Mascot score: 171. (C) Subunit composition of Psb34-PSII assembly intermediates analyzed by 2D-PAGE.

145 **Psb28 forms an extended beta hairpin structure that involves the D1 D-E loop and the**
 146 **CP47 C-terminus**

147 Psb28 binds on the cytosolic faces of the D1 and D2 subunits, directly above the Q_B binding
 148 site (Fig. 3A), which differs from the position that was previously predicted by mass
 149 spectrometry³⁷. Its binding induces the formation of an extended beta-hairpin structure that
 150 incorporates the central anti-parallel beta-sheet of Psb28, the C-terminus of CP47 and the D1
 151 D-E loop⁴⁶ (Fig. 3A). Binding of Psb28 to the C-terminus of CP47 also imparts a directionality
 152 to the assembly process. In the Psb28-free complex (PSII-M), the CP47 C-terminus blocks the

153 Psb28 binding site by interacting with the D1 D-E loop, thus preventing the reverse process and
154 perturbation of active PSII by Psb28. Using nuclear magnetic resonance (NMR) spectroscopy,
155 we performed chemical shift perturbation (CSP) experiments with recombinant Psb28 and a
156 synthetic peptide of the conserved CP47 C-terminus to characterize this interaction in detail
157 and determine the dissociation constant (K_D) (Fig. 3 and Fig. S4). The CSP measurements
158 indicated significant shifts with a chemical shift difference ($\Delta\delta$) of more than one standard
159 deviation located at strands $\beta 3$ and $\beta 4$ as well at the C-terminal region of Psb28 (Fig. 3C and
160 D). Upon peptide binding, resonances for several residues gradually appeared with increasing
161 peptide concentration, which were line-broadened beyond detection for the free form of Psb28.
162 This observation indicates a less dynamic and more rigid complex structure. This is further
163 supported by the heteronuclear Overhauser effect (NOE) data, which show that the C-terminus
164 of Psb28 becomes rigid from L108 to K112 upon CP47 peptide binding due to creation of an
165 intermolecular β -sheet (Fig. 3E). 2D-lineshape analysis was performed, yielding a K_D of
166 $53.92 \pm 0.41 \mu\text{M}$ and a dissociation rate k_{off} of $10.14 \pm 0.16 \text{ s}^{-1}$, which is consistent with the
167 observed slow-exchange in the NMR spectra (Fig. 3B). The affinity of Psb28 for full-length
168 CP47 and PSII might indeed be even higher due to additional contacts between Psb28 and the
169 D-E loop of D1 (Fig 3A).

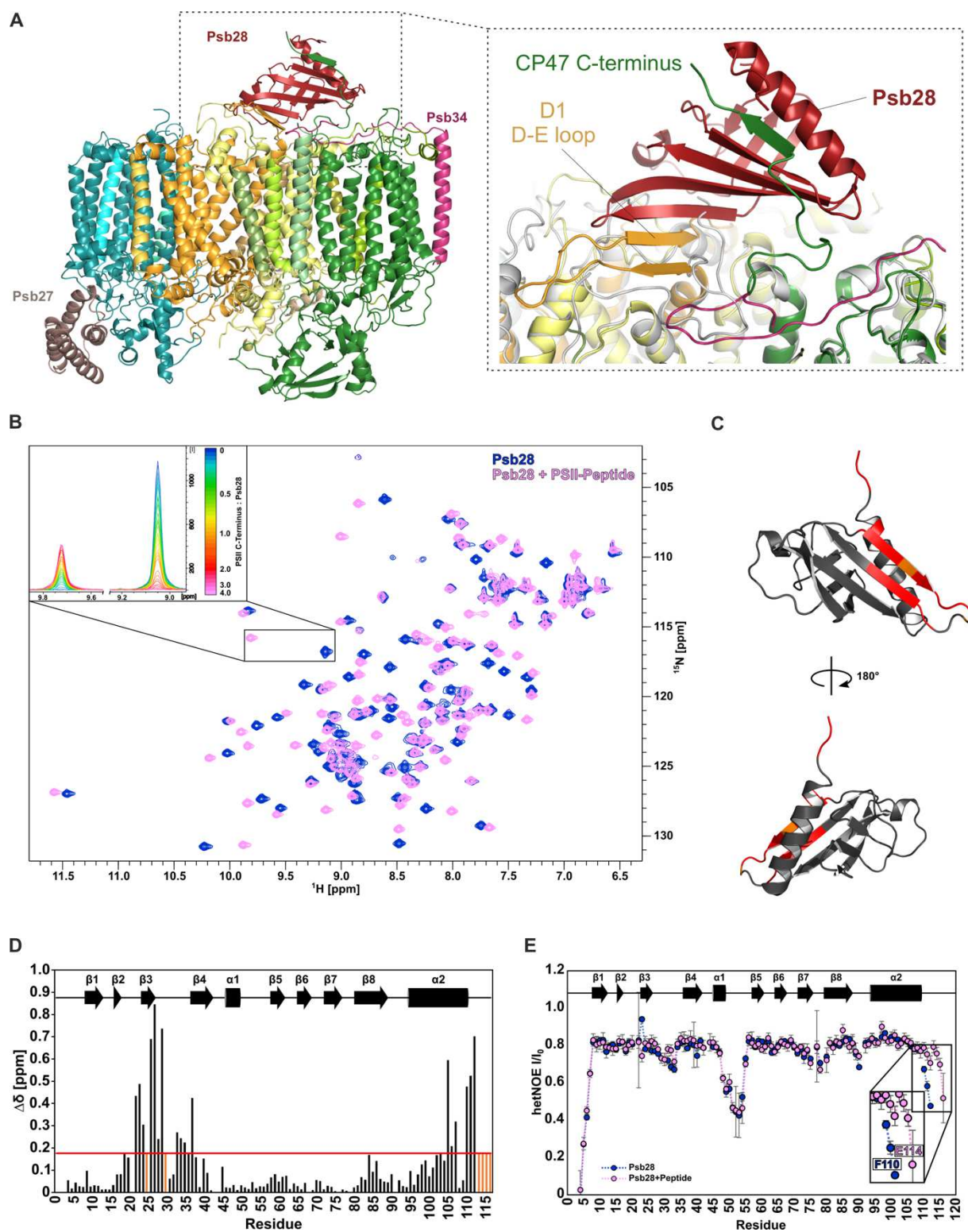


Fig. 3: The role of the CP47 C-terminus in binding of Psb28. (A). Binding of Psb28 at the cytoplasmic/stromal PSII surface (side view, colors correspond to Fig. 1) and continuation of the central Psb28 beta-sheet by the CP47 C-terminus and the D-E loop of D1 (dashed box). For comparison, mature monomeric PSII (PDB-ID 3KZI) is shown in gray. (B) Superimposed 2D ^1H - ^{15}N -HSQC spectra of free Psb28 (blue) and Psb28 bound to the C-terminal peptide of CP47 (magenta). Upper left inset: representation of slow exchange behavior for the proton amide resonance of T24, ranging from 126.9 ppm to 128.6 ppm in the ^{15}N dimension. (C) CSPs of more than one SD projected onto the model representation of Psb28. (D) Weighted $^1\text{H}/^{15}\text{N}$ chemical shift perturbations observed

for Psb28 upon binding to the CP47 peptide. Red line indicates one standard deviation (SD), residues that yield resonances only in the complex form are indicated in orange. **(E)** Backbone ^{15}N $\{^1\text{H}\}$ -heteronuclear NOE of free Psb28 (*blue*) and Psb28 bound to the C-terminal region of the CP47 peptide (*magenta*). Smaller I/I_0 ratios correspond to regions that exhibit dynamics on the pico- to nanosecond timescale.

170 **Psb28 binding prevents full association of CP43 and distorts the Q_B binding pocket**

171 Binding of Psb28—with support of Psb34—causes major structural perturbations at the PSII
172 acceptor side (Supplementary Movies 1 and 2), which mainly involve the D-E loops of the
173 central D1 and D2 subunits. Comparison of the CP43 structure in PSII-I with that in our
174 PsbJ-free control PSII-M (Fig. 4A-D) or with that in mature monomeric PSII (PDB-ID 3KZI)
175 (Fig. 4C and D) reveals several differences. The CP43 C-terminus is not resolved in PSII-I,
176 probably due to an immature position of the last transmembrane helix of CP43 and an altered
177 conformation of the D1 D-E loop, which may prevent binding of the CP43 C-terminus to the
178 cytoplasmic PSII surface (Fig. 4B). This region is close to the loop between helices D and E of
179 the D2 subunit, which is also altered by binding of Psb28, as clearly shown by movement of
180 D2 Arg233 (Fig. 4B, Fig. S5A and B). After dissociation of Psb28, the CP43 module undergoes
181 a rigid body rotation where it clicks into place (Fig. 4B-D, Supplementary Movie 1), whereas
182 binding of PsbJ and the extrinsic proteins PsbO, PsbV and PsbU during further maturation has
183 very little influence on the CP43 binding position (Fig. 4C and D). The part of PSII that
184 originates from RC47 shows almost no difference between PSII-I and mature PSII (Fig. 4D),
185 except for PsbE, which binds adjacent to PsbJ (Fig. 4C).

186 Most importantly, the structural changes in the D1 D-E loop may have a direct functional impact
187 on PSII electron transfer (Fig. 4E and F), as this region coordinates several important PSII
188 cofactors. In functional PSII, after charge separation at the reaction center P_{680} , electrons are
189 transferred via pheophytin to the bound plastoquinone (Q_A) and further to mobile plastoquinone
190 (Q_B). In our PSII-I structure, the Q_A site is fully assembled, and a well-resolved Q_A molecule is
191 bound (Fig. 4E and F, Fig. S5C and D). The nearby non-heme iron is also already in place in
192 PSII-I (Fig. 4E and F, Fig. S5E and F). The Q_B binding site of the PSII-M control is comparable
193 to mature PSII, although it is not occupied by Q_B in our preparation (Fig. S5G). In contrast, the
194 Q_B binding site of PSII-I is immature due to the Psb28- and Psb34-induced structural changes
195 in the D1 D-E loop (Fig. 4E and F, Fig. S5H). Notably, D1 Phe265, which coordinates the head
196 group of Q_B in mature PSII, is clearly at a different position²¹ (Supplementary Movie 2).

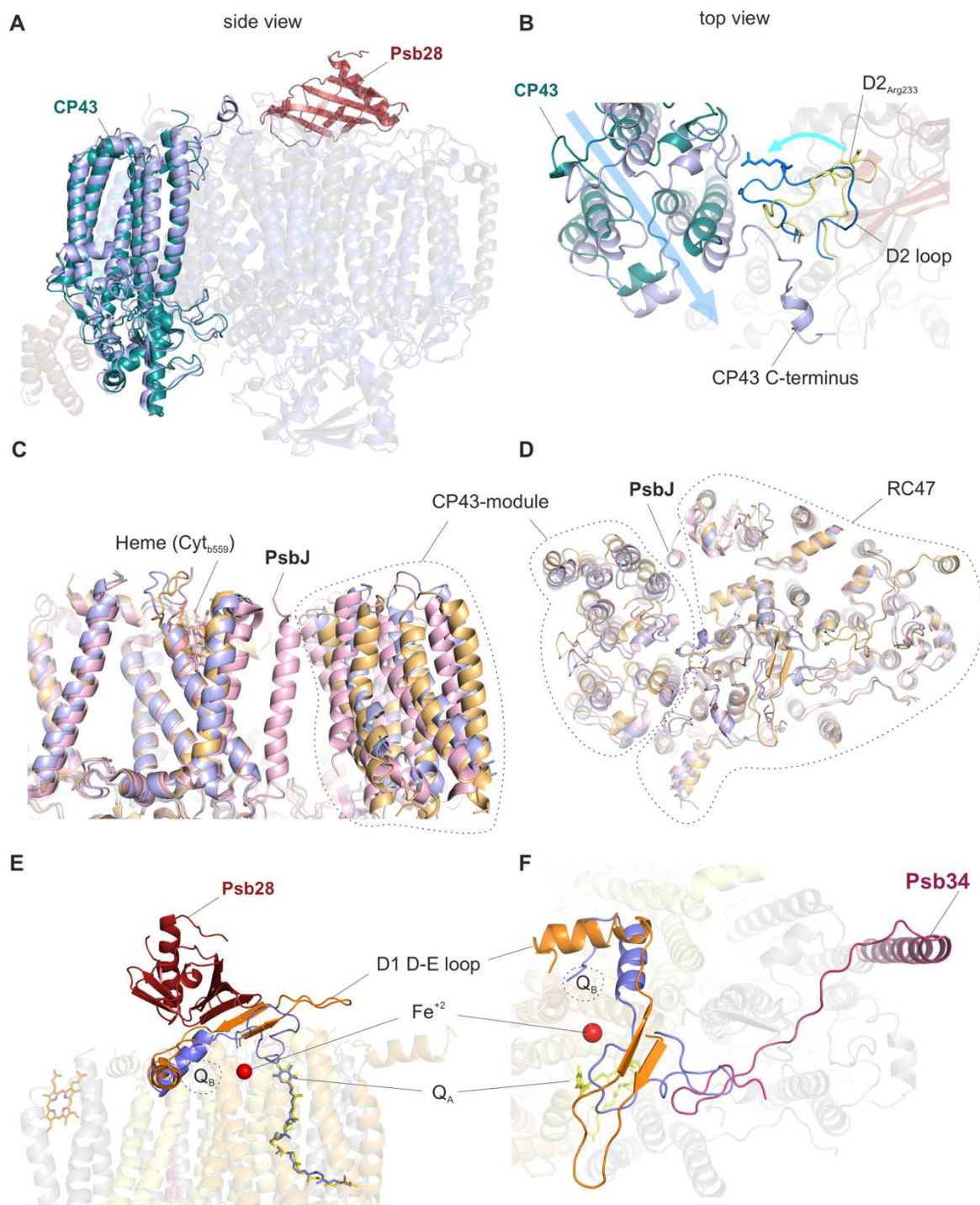


Fig. 4. Structural changes of the D1 and D2 D-E loops induced by binding of Psb28 and Psb34. (A) Side view of the CP43 antenna protein in PSII-I (*teal*) and the PSII-M control (*light blue*). (B) Structural changes between PSII-I and the PSII-M control in the cytoplasmic D2 D-E loop (*yellow*: PSII-I, *blue*: PSII-M) and attachment of CP43 (*teal*: PSII-I, *light blue*: PSII-M control) (top view). Details of the structural changes in the D2 loop are shown in Fig. S5A and B. (C) Side view and (D) top view of the PSII-I structure (*orange*) compared to the PSII-M control (*light blue*) and mature monomeric PSII (*light red*, PDB-ID 3KZI). (E) Side view and (F) top view of the Psb28-induced structural changes in the D1 D-E loop (*orange*) and perturbation of the Q_B binding site compared to PSII-M (*light blue*), which lacks the assembly factors. Q_A is shown in *yellow* (PSII-I) or *light blue* (PSII-M), respectively. See Fig. S5C-H for enlarged views of the Q_A and Q_B binding site and the adjacent non-heme iron.

197 **Binding of Psb28 protects PSII during biogenesis**

198 A more detailed analysis of the structural environment close to the Q_A/Q_B binding sites revealed
199 differences in the coordination and the hydrogen-bond network of the adjacent non-heme iron,
200 which also indicate functional consequences for PSII electron transfer and charge
201 recombination processes. In mature PSII, the non-heme iron is coordinated by four histidine
202 residues and bicarbonate as the fifth ligand (Fig. 5A and C), whereas in PSII-I, the bicarbonate
203 molecule is replaced by the E241 side-chain of D2 (Fig. 5B and D, Fig. S5E and F,
204 Supplementary Movie 3). Other residues, including D1 E244 and Y246, which bind to the
205 bicarbonate molecule in mature PSII (Fig. 5A), are also displaced in PSII-I due to the
206 conformational change of the D1 D-E loop (Fig. 5B, Fig. S5E and F, Supplementary Movie 3).
207 Binding of bicarbonate is important for PSII efficiency⁴⁷, as it lowers the redox potential of
208 (Q_A/Q_A^-) to favor forward electron transport^{48,49}. If charge recombination occurs, the lower
209 redox potential favors indirect charge recombination via $P^{*+}/Pheo^{\bullet-}$. This back reaction yields
210 triplet chlorophyll and subsequently singlet oxygen⁴⁹, a highly oxidizing species. Changes in
211 the redox potential of (Q_A/Q_A^-) have been proposed to tune the efficiency of PSII depending on
212 the availability of CO_2 as the final electron acceptor and thereby protect PSII under low CO_2
213 conditions⁴⁹. Therefore, we used flash-induced variable fluorescence to measure electron
214 transfer in the PSII-I assembly intermediate and inactivated PSII, both of which lack a
215 functional OEC (Fig. 5E, Fig. S6A and B). The fast component is assigned to PSII centers with
216 fast reoxidation of Q_A^- by properly bound Q_B , the middle component is caused by PSII
217 complexes with inaccurately bound Q_B , and the slow component is associated with centers that
218 do not contain Q_B and instead reoxidize Q_A^- through charge recombination with the Mn_4CaO_5
219 cluster⁵⁰. Fully functional PSII showed typical Q_A^- reoxidation, which is primarily due to fast
220 electron transfer to Q_B (Fig. 5E, blue trace). Addition of DCMU blocks electron transfer to Q_B
221 in active PSII, thereby promoting slow $S_2Q_A^-$ charge recombination (Fig. S6B, blue trace).
222 Removal of the OEC increases the Q_A redox potential⁵¹ and promotes very slow $Q_A^-TyD^+$
223 recombination (Fig. 5E, black trace)⁵², which is influenced only minimally by binding of DCMU
224 (Fig. S6B, black trace). PSII-I shows a different behavior (Fig. 5E, Fig. S6B red trace); ~60%
225 of the PSII-I centers decay within 1 s, whereas ~40% decay in PSII (-OEC). To determine
226 whether the replacement of bicarbonate by glutamate affects the energetics of the redox couple
227 Q_A/Q_A^- , we measured the formation of 1O_2 by EPR spectroscopy using the spin probe TEMPD.
228 The data clearly show that 1O_2 formation is reduced by ~30% in PSII-I compared to inactivated
229 PSII (-OEC), which contains bicarbonate (Fig. 5F).

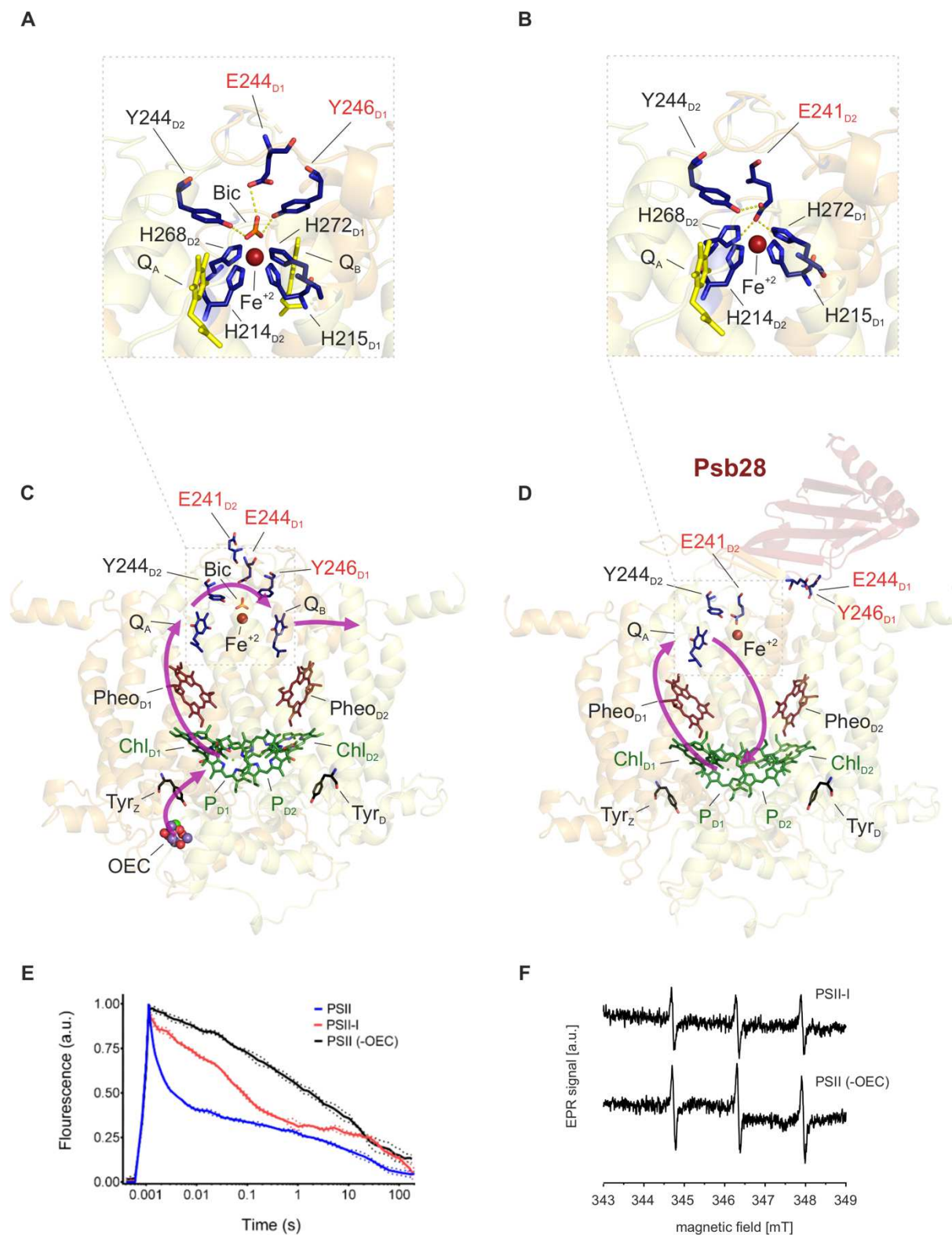


Fig. 5: Binding of Psb28 displaces bicarbonate as a ligand of the non-heme iron and protects PSII from damage. (A) The electron transfer from PQ_A to PQ_B is coordinated by the non-heme iron (Fe^{2+}), with the binding of bicarbonate (Bic) serving as a regulatory mechanism⁴⁹ in mature PSII (PDB-ID 3WU2). (B) Binding of Psb28 to the PSII-I assembly intermediate induces a conformational change in the cytoplasmic D2 D-E loop, where the side chain of Glu241 replaces bicarbonate as a ligand of the non-heme iron. The respective fits of the non-heme iron binding sites are shown in Fig. S5E and F. A similar coordination is also found in non-oxygenic bacterial reaction centers⁵³ (Fig. S6C). (C) Electron transfer (purple arrows) in mature PSII. Light-induced charge separation at the reaction center chlorophylls (P_{D1} , P_{D2} , Chl_{D1} , Chl_{D2}) leads to electron transfer via pheophytin ($Pheo_{D1}$) and plastoquinone A (Q_A) towards Q_B . The electron gap at the reaction center is filled by the oxygen

evolving complex (OEC). **(D)** Reoxidation of Q_A^- by direct and safe charge recombination is favored in the PSII assembly intermediate, as indicated by the purple arrows. **(E)** Flash-induced fluorescence decay of PSII. Blue lines represent active PSII, black and red represent PSII without functional OEC and PSII-I respectively. Dotted corridors depict SD ($n = 3$). **(F)** The protective role of Psb28 binding was further confirmed by EPR spectroscopy using the spin probe TEMPD, which is specific for 1O_2 , the major reactive oxygen species in PSII generated by triplet chlorophyll (3P). Inactivated PSII without functional Mn_4CaO_5 cluster (-OEC) was used as control.

230 **Psb27 binds in a remote position to loop E of CP43 at the luminal PSII surface**

231 Psb27 binds to the luminal side of the PSII complex, adjacent to loop E of the CP43 subunit
232 (Fig. 6A). In contrast to previously proposed models^{54,55}, the binding site of Psb27 has little
233 overlap with the binding sites of the extrinsic subunits (PsbO, PsbV and PsbU) and has at least
234 no direct impact on the Mn_4CaO_5 cluster binding site (Fig. 6A and B). Instead, Psb27 is bound
235 at a remote position that might be occupied by CyanoQ in the mature complex⁵⁶. This
236 localization of Psb27 does not support previous functional models in which bound Psb27
237 prevents the binding of the extrinsic subunits or plays a direct role in Mn_4CaO_5 cluster assembly
238 ^{33,54}. However, Psb27 might stabilize loop E of CP43 in the unassembled state and facilitate its
239 binding to the D1 subunit. This is of particular importance, as loop E of CP43 provides Arg345
240 and Glu342, two ligands of the Mn_4CaO_5 cluster in mature PSII (Fig. 6B, dashed box).
241 Moreover, in the Psb27-bound state (PSII-I), the D1 C-terminus, which is directly involved in
242 coordination of the Mn_4CaO_5 cluster²¹, is bound away from the cluster (Fig. 6C, Fig. S7). Thus,
243 our PSII-I structure reveals not only how the Psb27 protein binds to CP43 and thus stabilizes it
244 prior to attachment, but also indicates an indirect role for CP43 in maturation of the oxygen
245 evolving cluster that is consistent with functional data from previous studies^{31,34,40}.

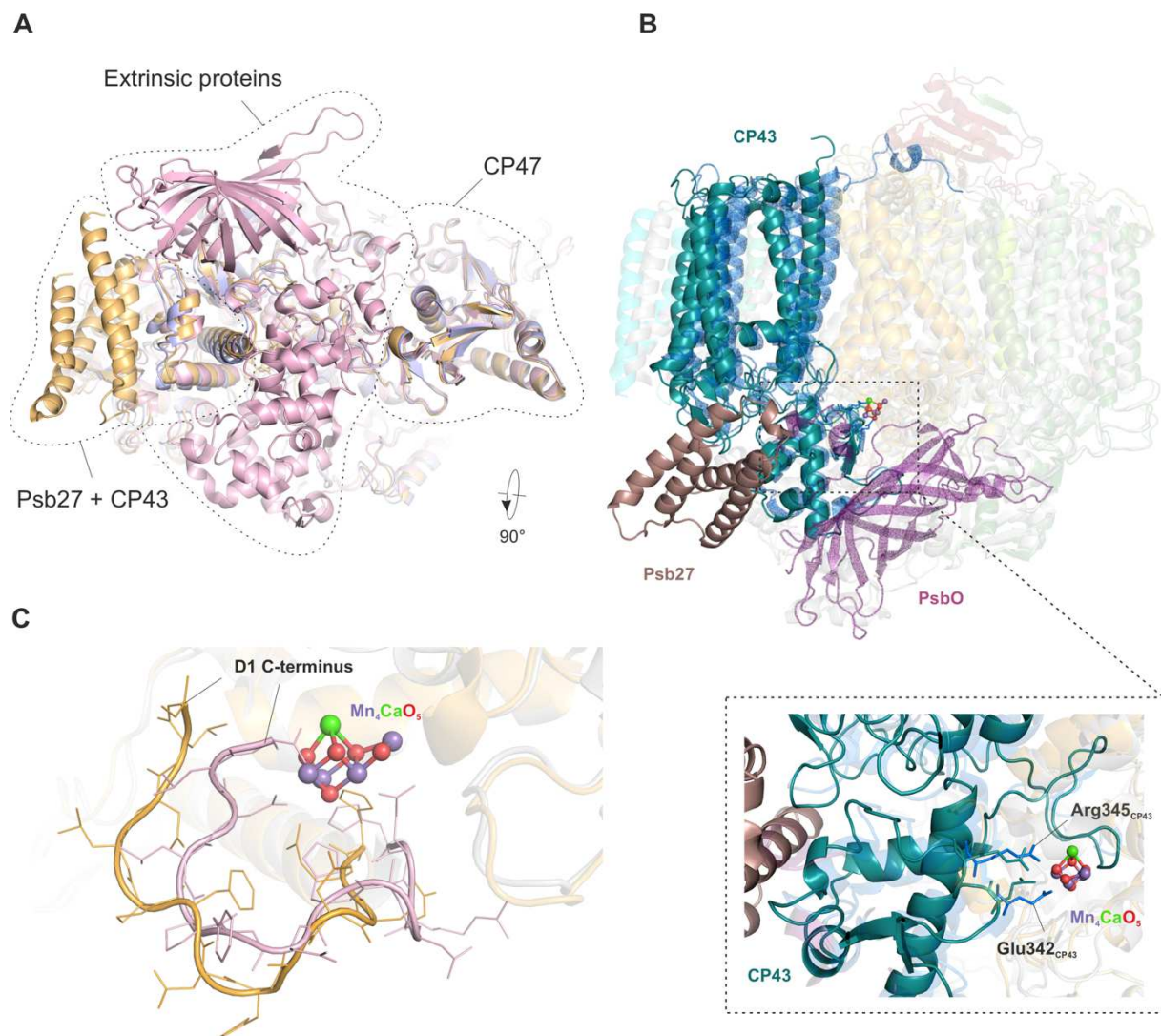


Fig. 6: The role of Psb27 in Mn_4CaO_5 cluster assembly. (A) Bottom view of the luminal PSII surface for PSII-I (*orange*), the PSII-M control (*light blue*) and mature monomeric PSII (PDB-ID 3KZI) (*light red*). (B) Side view of CP43 (*teal*) and Psb27 (*brown*) in PSII-I, as well as of CP43 (*blue*) and PsbO (*purple*) in mature monomeric PSII (PDB-ID 3KZI). Dashed box: CP43 E loop with residues Arg345 and Glu342 (shown as sticks), which are involved in coordination of the Mn_4CaO_5 cluster. We changed the numbering of CP43 residues due to a corrected N-terminal sequence (www.UniProt.org). The residues correspond to Arg357 and Glu354 in previous publications. The high-resolution structure of the Mn_4CaO_5 cluster is taken from Umena et al. 2011 (PDB-ID 3WU2). (C) Position of the D1 C-terminus in PSII-I (*orange*) and mature monomeric PSII (PDB-ID 3KZI) (*light red*).

246 **The immature Mn_4CaO_5 cluster binding site of PSII-I contains a single, positively charged**
 247 **ion**

248 The unique Mn_4CaO_5 cluster is a key feature of PSII that splits water into oxygen and protons.
 249 However, our PSII-I complex does not show any oxygen-evolving activity, suggesting that the
 250 oxygen evolving complex (OEC) is not fully assembled. In mature PSII, the Mn_4CaO_5 cluster
 251 is submerged in the complex and additionally capped by the extrinsic subunits PsbO, PsbU and
 252 PsbV (Fig. 6A and B). In our PSII-I structure, these subunits are absent, which leaves two parts
 253 of the CP43 E-loop (residues 320-327 and 397-404) in a flexible conformation, exposing the

254 binding site of Mn_4CaO_5 cluster to the lumen. There is no strong density feature at this position
255 that would correspond to the fully assembled metal-redox cofactor. Thus, our PSII-I structure
256 provides a model for an immature OEC. By comparing our structure with the high-resolution
257 crystal structure of mature PSII²¹ (PDB-ID 3WU2) provides insights into the first-steps of OEC
258 biogenesis (Fig. 7).

259 The D1 C-terminus is one of the key features for the formation of the of OEC, as it provides
260 several essential charged residues that are responsible for coordination of the chloride ion and
261 the Mn_4CaO_5 cluster (Fig. 7A, B and D). The density for these C-terminal residues is weak in
262 our PSII-I map, but traceable (Fig. S7A), indicating a flexibility that confirms the absence of
263 the OEC. Compared to the mature complex, the last 12 residues of the C-terminal tail of D1
264 would need to undergo significant conformational changes to bring the side chains of Glu333,
265 His337, Asp342, and the Ala344 C-terminus into the correct position to coordinate the
266 Mn_4CaO_5 cluster (Supplementary Movie 4).

267 Moreover, we identify a clearly visible density at the position of the chloride ion, which is
268 coordinated by Lys317 (D2) and the hydrogen atom of the backbone nitrogen of Glu333 (D1)
269 in mature PSII (Fig. 7B and E). Despite the similar position, the Cl^- is coordinated by the
270 nitrogen atom of the ring of adjacent His332 (D1) in PSII-I (Fig. 7A and E, Fig. S7D).
271 Surprisingly, we identified another density in the area where the Mn_4CaO_5 cluster is located in
272 mature PSII (Fig. 7A-C and F, Fig. S7C). However, this density is not large enough to reflect
273 the whole cluster. Based on its size and interaction partners (Fig. 7F), it corresponds to one
274 positively charged ion. In the structural context, this ion is most likely Mn^{2+} , but it could also
275 be Ca^{2+} or any other positively charged ion.

276 This ion is coordinated by the side chains of D1 Asp170, Glu189, and His332, which are already
277 in similar positions compared to mature PSII. Glu342 and Arg345 of CP43, which are both
278 involved in the Mn_4CaO_5 cluster coordination, are also already pre-positioned through the
279 interaction between Arg345 with D1 Asp170 (Fig. 7G). However, there are still significant
280 conformational changes necessary for the transition from PSII-I to mature PSII, as highlighted
281 in Figure 7D and G, as well as in Supplementary Movie 4. The D1 C-terminal tail must bring
282 the side chains of Glu333, His337 and Asp342, as well as the C-terminus of Ala344, into correct
283 alignment to coordinate the Mn_4CaO_5 cluster. In addition, the C-terminal tail of D2 needs to
284 flip towards the D1 C-terminus (Fig. 7C, Fig. S7B, Supplementary Movie 4). In summary,
285 PSII-I is characterized by only one positive charged ion bound instead of the complete
286 Mn_4CaO_5 cluster, resulting in significantly different conformations of the D1 and D2 C-termini

287 compared to the structural model containing a mature Mn_4CaO_5 cluster. However, the PSII-I
 288 structure seems to be prepared to accept the Mn_4CaO_5 cluster, as indicated by the above
 289 described similarities in side chain positioning.

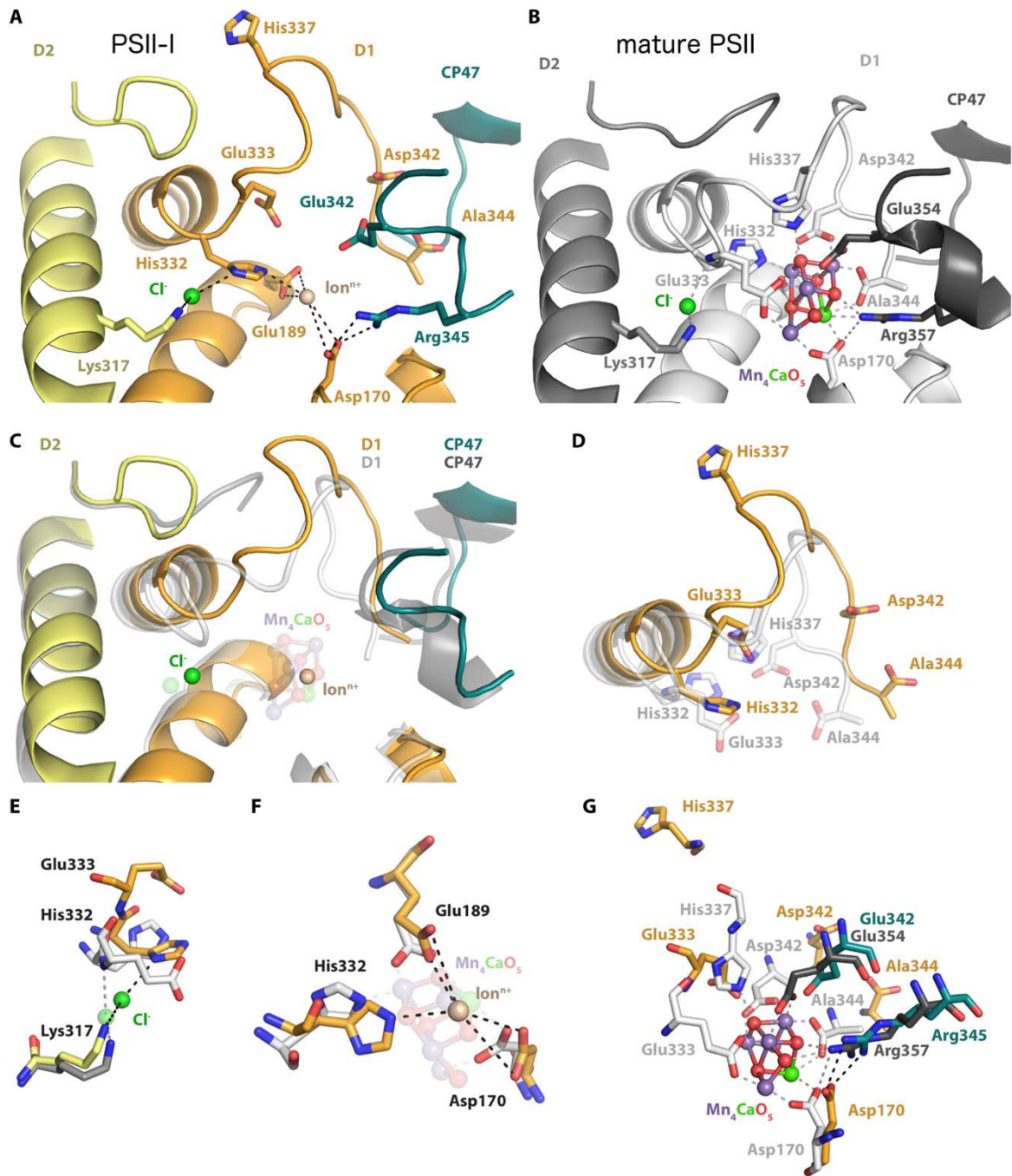


Figure 7: Conformational changes within the active site of the Mn_4CaO_5 cluster. The Mn_4CaO_5 cluster performs PSII's unique water-splitting reaction. (A) The active site of the Mn_4CaO_5 cluster is resolved within our PSII-I structural model but is not yet oxygen-evolving. (B) Crystal structure of the oxygen-evolving, mature PSII (PDB-ID 3WU2, resolution 1.9 Å). (C) Overlay of both structures, illustrating significant differences in the backbone conformation of the D1 and D2 C-terminal tails. (D) Accompanying side chain rearrangements of the D1 C-terminus. The Cl^- (E), Ion^{n+} (F) and Mn_4CaO_5 (G) cluster coordination partners are compared in detailed. The validation of the fit to density for the structural details shown here is provided in Figure S7.

290 Discussion

291 PSII biogenesis is a complex process that requires the action of specific assembly factors. These
292 auxiliary proteins are not present in the mature complex and interact only transiently with
293 specific subunits or preassembled PSII intermediates. Although more than 20 factors have been
294 identified and allocated to specific transitions, their precise molecular function in PSII assembly
295 remains elusive in almost all cases. Our study provides the first detailed molecular insights into
296 the function of PSII assembly factors Psb27, Psb28 and Psb34, which are involved in an
297 important transition prior to activation of the OEC. The determined binding positions of Psb27
298 and Psb28, which are two of the most studied PSII assembly factors, disprove all previous
299 Psb27 and Psb28 binding models and exclude Psb27 from direct involvement in OEC
300 maturation^{54,55,57-61}.

301 Binding of Psb28 and Psb34 to the cytoplasmic side of PSII induces large conformational
302 changes in the D1 D-E loop (Fig. 4), which has been identified previously as an important
303 location for PSII photoinhibition and D1 degradation^{62,63}. Structural changes observed in the
304 PSII-I Q_B binding pocket and coordination of the non-heme iron suggest a functional impact
305 on PSII electron transfer to protect the immature complex until water splitting is activated. In
306 particular, D2 Glu241 replacing bicarbonate as ligand of the non-heme iron by suggests a
307 regulatory role, as binding of bicarbonate was proposed to tune PSII efficiency by changing the
308 redox potential of (Q_A/Q_A⁻)^{48,49}. As a functional consequence, PSII-I generates less singlet
309 oxygen compared to inactive PSII (Fig. 5F).

310 Interestingly, the coordination of the non-heme iron in PSII-I resembles that in non-oxygenic
311 bacterial reaction centers (BRCs)⁵³ (Fig. S6C). In BRCs, the fifth ligand of the non-heme iron
312 is provided by E234 of the M subunit⁶⁴, and mutagenesis of this residue induces changes in the
313 free energy gap between the P^{•+}/Q_A^{•-} radical pair⁶⁵. These findings indicate that the
314 environment of the non-heme iron is important for regulation of forward electron transfer to Q_B
315 versus charge recombination⁴⁸. Therefore, we speculate that during biogenesis, PSII switches
316 to a mechanism that usually operates in non-oxygenic bacterial reaction centers.

317 The Psb27-bound and -unbound structures do not differ substantially (Fig. 6B), suggesting a
318 rather subtle action in PSII biogenesis. Previous work demonstrated that Psb27 is already bound
319 to free CP43³¹, where it might protect free CP43 from degradation or stabilize the E-loop in a
320 specific conformation to chaperone the subsequent association with the RC47 complex. This
321 step is crucial for preparing the binding site of the Mn₄CaO₅ cluster, as the CP43 E-loop
322 provides two ligands of the cluster. Further OEC assembly is a multistep process that requires

323 a functional upstream redox chain for the oxidation of Mn^{2+} to build up the cluster's μ -oxo
324 bridges between the manganese atoms⁶⁶⁻⁶⁹. The mechanistic and structural details of this
325 photoactivation process are not yet understood. In the consensus 'two quantum model', a single
326 Mn^{2+} ion bound to the high-affinity site (HAS) is oxidized to Mn^{3+} . This initiating light-
327 dependent step is followed by a slow light-independent phase and further fast light-dependent
328 steps in which the remaining Mn^{2+} ions are oxidized and incorporated. Understanding the light-
329 independent slow phase is key to unraveling the mechanism of photoactivation.

330 Previous structural studies aimed to obtain mechanistic insights into the dark-rearrangement by
331 removing the Mn_4CaO_5 cluster from fully assembled PSII, either by depleting it directly from
332 PSII crystals by chemical treatment⁷⁰ or by cryo-EM single particle analysis in manganese- and
333 calcium-free buffer⁷¹. The X-ray structure was indeed missing the Mn_4CaO_5 cluster, but the D1
334 C-terminus followed mostly the same trajectory as found in the mature PSII-dimer structure.
335 The authors suggested that the D1 C-terminus might not rearrange during Mn_4CaO_5 cluster
336 assembly. However, the crystal structure was dimeric and still had the extrinsic subunits PsbO,
337 PsbU, and PsbV bound. It is known that these subunits are typically not associated with
338 Mn_4CaO_5 cluster-depleted PSII. Thus, the structure might be artificially stabilized by crystal
339 packing forces. The cryo-EM structure, on the other hand, revealed a monomeric PSII that lacks
340 extrinsic subunits and the Mn_4CaO_5 cluster⁷¹. This structure is more similar to our PSII
341 biogenesis intermediate PSII-I, as PsbY, PsbZ and PsbJ are also missing. The PsbJ subunit is
342 surprising; it is an integral subunit of PSII and should not be easily detached, yet it is missing
343 from this structure and we deleted it to stabilize our PSII-I complex. These observations might
344 indicate a more specific and regulatory role of PsbJ in PSII biogenesis. Additionally, the D1 C-
345 terminus is disordered in this previous cryo-EM structure, and the authors suggest that the dark-
346 rearrangement involves a transition from a disordered to an ordered state.

347 Our structure now reveals the fate of the D1 C-terminus with the assembly factor Psb27 bound.
348 The D1 C-terminus follows a different trajectory compared to the mature PSII. Thus, we
349 provide structural evidence that the slow dark-rearrangement involves a conformational change
350 of the D1 C-terminus rather than the previously proposed disorder-to-order transition after
351 initial photoactivation⁷¹. Compared to mature PSII, twelve residues of the D1 C-terminal tail
352 must undergo significant conformational changes to bridge the side chains of Glu333, His337
353 and Asp342, as well as to bring the C-terminus of Ala344 in the correct position to coordinate
354 the Mn_4CaO_5 cluster (Fig. 6C and 7D, Supplementary Movie 4), which is consistent with
355 previous models^{69,72,73}. We also identified a single positively charged ion in our PSII-I
356 structure, coordinated by Asp170, Glu189 and His332 of D1 (Fig. 7F), at the position of the

357 Mn₄CaO₅ cluster of mature PSII. This binding site most likely corresponds to the long-sought
358 single high-affinity site (HAS), where the first Mn²⁺ binds prior to the first photoactivation step
359 in OEC biogenesis⁷⁴. However, we cannot exclude binding of Ca²⁺, which was shown to bind
360 with a much lower affinity^{72,75}, or any other positive charged ion at this position. Nevertheless,
361 Asp170 has been identified as the most critical residue for the HAS^{76,77}, which supports our
362 hypothesis. Further photoactivation steps occur presumably after cooperative binding of
363 calcium and manganese. The binding of the extrinsic subunit PsbO, potentially after release of
364 Psb27 and maturation of the WOC, is the next step of the PSII assembly line *in vivo*, which
365 leads to the next unsolved question in PSII biogenesis: what triggers the release of an assembly
366 factor? For Psb27, its detachment might be promoted by the binding of PsbO, as their binding
367 sites partially overlap.

368 Membrane protein complexes play a fundamental role in bioenergetics to sustain and proliferate
369 life on Earth. They drive the light-to-chemical energy conversion in photosynthetic organisms
370 and are essential for energy supply in heterotrophs. These highly complex molecular machines
371 are assembled from numerous single proteins in a spatiotemporally synchronized process that
372 is facilitated by a network of assembly factors. These auxiliary proteins are the key players of
373 Nature's assembly lines. Our PSII-I cryo-EM structure reveals the first molecular snapshot of
374 PSII biogenesis and, accompanied by our spectroscopic and biochemical analyses, provides
375 clear mechanistic insights into how three assembly factors (Psb27, Psb28 and Psb34) coordinate
376 the stepwise construction of this powerful catalyst of life.

377 **Methods**

378 **Cultivation of *Thermosynechococcus elongatus* BP-1**

379 Cell growth and thylakoid membrane preparation were performed as described previously⁷⁸. In
380 brief, *T. elongatus* mutant strains (Δ psbJ psbC-TS and psb34-TS) were grown in BG-11 liquid
381 medium inside a 25-liter foil fermenter (Bioengineering) at 45°C, 5% (v/v) CO₂-enriched air
382 bubbling and 50-200 μ mol photons m⁻² s⁻¹ white light illumination (depending on the cell
383 density). Cells were harvested at an OD₆₈₀ of ~ 2 after 5-6 days of cultivation and concentrated
384 to ~ 0.5 l using an Amicon DC10 LA hollow fiber system, pelleted (3500 rcf, 45 min and 25
385 °C) and resuspended in 150 ml of Buffer D (100 mM Tris-HCL, pH 7.5, 10 mM MgCl₂, 10
386 mM CaCl₂, 500 mM mannitol and 20% (w/v) glycerol). The harvested cells were flash frozen
387 in liquid nitrogen and stored at -80 °C until further use.

388 **Preparation of *T. elongatus* mutant strains**

389 *Thermosynechococcus elongatus* Δ psbJ psbC-TS was generated based on the previously
390 described strain *T. elongatus* Δ psbJ³⁵ that was transformed with the plasmid pCP43-TS. The
391 plasmid is based on pCP34-10His³³. The His-tag sequence was exchanged with TwinStrep-tag
392 by PCR using the primers CP43TS_rev (5' CCGGATATCTTACTTCTCAAATTGCGGAT
393 GAGACCACGCAGAACCACCAGAACCACCGCCGCTGCCGCCGCCTTTTTTCGAACTG
394 CGGGTGGCTCC 3') and NTCP43 (5' TGCTCTAGAATGAAAACCTTTGTCTTCCCAGA
395 3'). The resulting PCR product was ligated back into an empty pCP34-10His backbone using
396 XbaI and EcoRV restriction endonucleases. *T. elongatus* BP-1 cells were transformed as
397 described previously⁷⁹. Mutant colonies were selected by frequent re-plating onto agar plates
398 with increasing antibiotic concentrations, stopping at 8 μ g/ml of chloramphenicol and 80 μ g/ml
399 of kanamycin. Complete segregation of the mutant was confirmed by PCR with the primers
400 CTCP43DS (5' CCGCTCGAGACCATCCAAGCTTGGCAGCA 3') and NTCP43 (5'
401 TGCTCTAGAATGAAAACCTTTGTCTTCCCAGA 3'). *T. elongatus* psb34-TS was generated
402 by transformation with the plasmid pPsb34-TS. The plasmid DNA was obtained from
403 TwistBioscience. It consisted of psb34 (tsl0063) with a C-terminal TwinStrep-tag and a
404 kanamycin resistance cassette, flanked by tsl0063-upstream and downstream regions (900 bp
405 each). *T. elongatus* BP-1 cells were transformed⁷⁹ and mutant selection took place³³. Complete
406 segregation of the mutant was verified by PCR. The primers used were tsl0063-up-for (5'
407 CATATGGTCTCGCAATTATTTGCCATGC 3') and tsl0063-down-rev (5' GGTACCCCG
408 ACACAGTTGATCACCGC 3').

409 **Purification of photosystem II assembly intermediates**

410 Thawed cells were diluted in 100 ml of Buffer A (100 mM Tris-HCL, pH 7.5, 10 mM MgCl₂
411 and 10 mM CaCl₂) and pelleted again (21 000 rcf, 20 min and 4°C). The pellet was resuspended
412 in 100 ml of Buffer A with 0.2% (w/v) lysozyme and dark incubated for 75-90 min at 37 °C.
413 This was followed by cell disruption by Parr bomb (Parr Instruments Company) and pelleting
414 (21 000 rcf, 20 min and 4°C). All following steps were performed under green illumination.
415 The pellet was resuspended in 150 ml of Buffer A and pelleted again (21 000 rcf, 20 min and
416 4°C). This step was repeated three times, with the last resuspension in 80 ml of Buffer B (100
417 mM Tris-HCL, pH 7.5, 10 mM MgCl₂, 10 mM CaCl₂ and 500 mM mannitol). The isolated
418 thylakoids were flash frozen in liquid nitrogen and stored at -80 °C.

419 Strep-Tactin-affinity purification of PsbC-TS and Psb34-TS assembly intermediates were
420 performed under green illumination. Membrane protein extraction was performed as described
421 previously⁷⁸, with certain adaptations. Thylakoid membranes were supplemented with 0.05%
422 (w/v) n-Dodecyl β-maltoside (DDM) (Glycon) and pelleted (21000 rcf, 20 min and 4°C). The
423 sample was resuspended in extraction buffer (100 mM Tris-HCL, pH 7.5, 10 mM MgCl₂, 10
424 mM CaCl₂, 1.2% (w/v) DDM, 0.5% (w/v) sodium-cholate and 0.01% (w/v) DNase) to a final
425 chlorophyll concentration of 1 mg/ml and incubated for 30 min at 20 °C. The solubilized
426 membrane proteins were ultra-centrifugated (140000 rcf, 60 min and 4 °C) and NaCl was added
427 to the supernatant to a final concentration of 300 mM.

428 The supernatant was filtered through a 0.45 μm filter and applied to a 5 ml Strep-Tactin
429 Superflow HC column (IBA Lifesciences), equilibrated in Buffer W (100 mM Tris-HCL, pH
430 7.5, 10 mM MgCl₂, 10 mM CaCl₂, 500 mM mannitol, 300 mM NaCl and 0.03% (w/v) DDM)
431 at a flowrate of 3 ml/min. The column was washed with Buffer W until a stable baseline (A₂₈₀)
432 was reached. Strep-tagged protein complexes were eluted by an isocratic elution with Buffer E
433 (100 mM Tris-HCL, pH 7.5, 10 mM MgCl₂, 10 mM CaCl₂, 500 mM mannitol, 300 mM NaCl
434 2.5 mM desthiobiotin and 0.03% (w/v) DDM). The captured fractions were equilibrated in
435 Buffer F (20 mM MES, pH 6.5, 10 mM MgCl₂, 10 mM CaCl₂, 500 mM mannitol and 0.03%
436 (w/v) DDM) with a spin concentrator (Amicon, Ultra – 15, 100000 NMWL), flash-frozen in
437 liquid nitrogen and stored at -80 °C until analysis.

438 PsbC-TS containing assembly intermediates were further separated by ion exchange
439 chromatography (IEC). Captured elution fraction from the Strep-Tactin-affinity purification
440 were loaded onto a anion exchange column (UNO Q-6, Biorad) with a flowrate of 4 ml/min,
441 pre-equilibrated in Buffer F. Protein complexes were eluted by a liner gradient of MgSO₄ (0-

442 150 mM) using Buffer G (20 mM MES, pH 6.5, 10 mM MgCl₂, 10 mM CaCl₂, 500 mM
443 mannitol, 150 mM MgSO₄ and 0.03% (w/v) DDM). Fractions containing PSII assembly
444 intermediates were collected, concentrated to 100 – 10 μM reaction centers, using a spin
445 concentrator (Amicon, Ultra – 15, 100 000 NMWL), aliquoted, flash frozen in liquid nitrogen
446 and stored at -80 °C until further analysis.

447 **Protein Expression and Purification of Psb28**

448 The Psb28 expression plasmid was constructed by first amplifying psb28 from *T. elongatus*
449 genomic DNA, using primers TeloPsb28for (5' GGAATTCCATATGGGTGCAATGGCA
450 GAAATTC 3') and TeloPsb28rev (5' CGAATTCCCCGGGAGAGTTCTCAGACTTCTG 3').
451 Next, the amplified DNA was cloned into pIVEX2.3d using *NdeI/SmaI* to obtain
452 pIVEXPsb28His. Expression and purification of ¹⁵N-labelled Psb28 was carried out as
453 described previously⁸⁰ with certain adaptations. Overnight starter cultures were grown on agar
454 plates at 37 °C, supplemented with 1 % (w/v) glucose and 100 μg/ml ampicillin. The cell
455 material was then resuspended in 2 ml of M9 media⁸¹, and this was used to inoculate 500 ml of
456 M9 media with ¹⁵NH₄Cl as the only nitrogen source. Cultures were incubated at 37 °C under
457 vigorous shaking and at an OD₆₀₀ of 0.6, and expression was induced with addition of
458 isopropylthiogalactoside to a final concentration of 0.5 mM. After overnight incubation the ¹⁵N-
459 labelled Psb28 was isolated and purified as described for his-tagged CyanoP⁸⁰. The purity and
460 integrity of the protein samples were checked by SDS-PAGE (data not shown).

461 **Polyacrylamide Gel Electrophoresis**

462 Blue-native PAGE⁸² was used to assess the oligomeric state of the isolated PSII assembly
463 intermediates. Separation of protein complexes was carried out across a linear gradient of
464 polyacrylamide (acrylamide-bisacrylamide, 32:1) from 3.2 to 16% (w/v) in the separating gel.
465 This was overlaid with a 3% (w/v) polyacrylamide (acrylamide-bisacrylamide, 32:1) sample
466 gel. The gels were loaded with 40 μg of protein per lane. Electrophoresis was performed at 4
467 °C in a Mini-PROTEAN Tetra System (BioRad) at 100 V for 30 min with Blue Cathode Buffer
468 (15 mM BisTris-HCl, pH 7.0, 50 mM Tricine and 0.002% (w/v) Coomassie Brilliant Blue 250)
469 and at 170 V for an additional 90 min with Cathode Buffer (15 mM BisTris-HCl, pH 7.0 and
470 50 mM Tricine). The anode buffer was composed of 50 mM BisTris-HCl at pH 7.

471 Subunit composition was investigated by SDS-PAGE⁸³. Separation of polypeptide chains took
472 place on a 19% (w/v) polyacrylamide gel (acrylamide-bisacrylamide, 37.5:1), containing 9 M
473 urea and 4% (w/v) glycerol. The gel was loaded with 40 μg of denatured protein complex per
474 lane. The gels ran at 4 °C in a Mini-PROTEAN Tetra System (BioRad) at 35 mA per gel for 60

475 min. Fixation and visualization of polypeptide chains was performed with Coomassie Staining
476 Solution (45% (w/v) isopropanol, 10% (w/v) acetate and 0.2% (w/v) Coomassie Brilliant Blue
477 250).

478 **Mass spectrometry analysis**

479 PSII-I complexes were purified and desalted using Isolute C18 SPE cartridges (Biotage,
480 Sweden). The columns were first washed and equilibrated, the sample diluted in 0,1%
481 trifluoroacetic acid (TFA) and loaded onto the column. After washing with 2 ml 0.1% TFA, the
482 proteins were eluted with 500 μ l 80% acetonitrile (ACN), 20% water. The organic fraction was
483 lyophilized in a vacuum concentrator (Eppendorf, Germany), reconstituted in 0.1% TFA and
484 mixed in a 1:1 ratio with HCCA matrix solution (HCCA (alpha-cyano-4-hydroxycinnamic
485 acid) saturated in 50% ACN, 50% water and supplemented with 0.1% TFA). Subsequently, 1
486 μ l aliquots of the mixture were deposited on a ground steel MALDI target and allowed to dry
487 and crystallize at ambient conditions.

488 MS and MS/MS spectra were acquired on a prototype rapifleX MALDI-TOF/TOF (Bruker
489 Daltonics, Germany) in positive ion mode. The Compass 2.0 (Bruker Daltonics, Germany)
490 software suite was used for spectra acquisition and processing (baseline subtraction, smoothing,
491 peak picking), a local Mascot server (version 2.3, Matrixscience, UK) was used for database
492 searches against the *T. elongatus* proteome (UniProt, retrieved 4/2019) and BioTools 3.2
493 (Bruker Daltonics) was used for manual spectrum interpretation, de novo sequencing and peak
494 annotation.

495 **Flash-induced fluorescence decay measurements**

496 Flash-induced fluorescence decay was measured on a FL3500 Dual-Modulation Kinetic
497 Fluorometer (PSI Photon Systems Instruments). Reaction centers were excited with 625 nm
498 LEDs for both actinic (50 μ s) and measuring flashes. The first data point was collected 80 μ s
499 after the actinic flash. Data points were collected from 80 μ s to 50 or 200 s after the actinic
500 flash for measurements with whole cells and isolated PSII, respectively. 10 data points were
501 collected per logarithmic decade. Assays were performed at room temperature in the presence
502 and absence of 20, 100, 200 or 400 μ M 3-(3,4-dichlorophenyl)-1,1-dimethylurea (DCMU) with
503 5 min of dark incubation prior to measurement. Assays with isolated PSII complexes were
504 carried out with 200 nM reaction centers in activity buffer (100 mM KCl, 20 mM MES-KOH,
505 pH 6.5, 10 mM MgCl₂, 10 mM CaCl₂ and 0.03% (w/v) DDM).

506 **NMR Spectroscopy**

507 Typically, NMR samples contained up to 1 mM of protein in 20 mM Tris/HCl pH 8, 10%D₂O,
508 0.02% NaN₃, and DSS. NMR spectra were acquired at 298 K on Bruker DRX 600 and
509 AVANCE III HD 700 spectrometers. Backbone assignments for the free form of Psb28 were
510 obtained from three-dimensional HNCA^{84,85}, and CBCA(CO)NH⁸⁶ spectra. Side-chain
511 assignments were obtained from three-dimensional ¹H-¹⁵N HNHA⁸⁷, ¹H-¹³C-HCCH-TOCSY
512 ⁸⁸, ¹H-¹⁵N-HSQC-TOCSY⁸⁹, ¹H-¹⁵N-HSQC-NOESY⁹⁰, ¹H-¹³C-HSQC-NOESY⁹¹, and aromatic
513 ¹H-¹³C-HSQC-NOESY spectra. Spectra were processed with NMRPipe⁹² and analysed with
514 CcpNmr Analysis⁹³. NMR experiments for the complex form of Psb28 and the C-terminal
515 peptide of CP47 were carried out on a Bruker AVANCE III HD 700 spectrometer at 298 K in
516 20 mM Tris/HCl pH8, 10%D₂O, 0.02% NaN₃, and DSS. For the backbone assignments of the
517 complex, a 1 mM sample of [U-¹⁵N-¹³C]-enriched Psb28 was mixed with a three-fold excess of
518 peptide. Three-dimensional (3D) HNCA, HNCO^{84,85}, HN(CO)CACB⁹⁴, HNCACB^{95,96}, and
519 HN(CA)CO⁹⁷ were recorded with 16 scans and 25% non-uniform sampling (NUS).
520 (H)CC(CO)NH and H(CCCO)NH spectra^{98,99} were recorded with 64 scans and 25% NUS.
521 HNHA and ¹H¹⁵N-HSQC-NOESY spectra were recorded with 32 scans and 25% NUS as well
522 as traditional acquisition schemes, respectively. The mixing time for NOESY spectra was set
523 to 120 ms. In addition, heteronuclear two-dimensional ¹⁵N {¹H}-NOE data were recorded in
524 order to extract pico- to nanosecond dynamics^{100,101}. The titrations were carried out by adding
525 increasing amounts of a peptide stock solution to the NMR sample containing 0.138 mM of
526 protein and two-dimensional ¹H¹⁵N-HSQC spectra¹⁰² were recorded after thorough mixing of
527 the Psb28-CP47 carboxyterminal peptide solution. Spectra were processed with NMRPipe⁹²
528 and Psb28 ligand affinity calculations based on two-dimensional lineshape analysis were
529 carried out using the TITAN software package¹⁰³.

530 **Synthetic Peptide**

531 The carboxy-terminal peptide from residues 480-499 of CP47, which comprises the sequence
532 SGIDPELSPEQVEWGFYQKV and includes an acetylated amino-terminus, was purchased
533 from JPT Peptide Technologies GmbH, Germany. Peptide stock solutions of at least 6.07 mM
534 for titration experiments were prepared by dissolving the peptide in 20 mM Tris/HCl pH8.

535 **Removal of the PSII oxygen evolving cluster**

536 PSII without functional oxygen evolving cluster (OEC) was prepared by isolating PSII as
537 described by Grasse et al.⁴⁰, followed by removal of the extrinsic subunits according to Shen
538 and Inoue¹⁰⁴, with modifications. PSII was applied to a size exclusion column (Superdex 75

539 10/300 GL, GE Healthcare) pre-equilibrated in CaCl₂ buffer (10 mM MgCl₂, 20 mM MES-
540 NaOH, pH 6.5, 1 M CaCl₂, 0.03% (w/v) DDM). PSII particles lacking the extrinsic subunits
541 and the Mn₄CaO₅ cluster, which were eluted in the void volume, were collected and the buffer
542 was exchanged to activity buffer (100 mM KCl, 20 mM MES-KOH, pH 6.5, 10 mM MgCl₂,
543 10 mM CaCl₂ and 0.03% (w/v) DDM) using a spin concentrator (Amicon, Ultra – 15, 100 000
544 NMWL).

545 **Detection of singlet oxygen by the room temperature EPR spectroscopy**

546 Singlet oxygen was trapped using the water-soluble spin-probe 2,2,6,6-tetramethyl-4-
547 piperidone (TEMPD) hydrochloride¹⁰⁵ and measured with ESR300 (Bruker Biospin,
548 Rheinstetten, Germany). Samples (30 µg chl ml⁻¹) were illuminated for 1 min with red light
549 (RG 630) at 450 µmol quanta m⁻²s⁻¹ in 0.5 M mannitol, 10 mM CaCl₂, 10 mM MgCl₂, 20 mM
550 MES at pH 6.5. Spectra were recorded using a flat cell containing 200 µl sample. The
551 microwave power was 9.77 GHz and 14.07 mW with a modulation frequency of 86 kHz and
552 amplitude of 1.0 G. Each spectrum is an average of 8 scans, each with a sweep time of 10.5 s.

553 **Cryo-electron microscopy**

554 For cryo-EM sample preparation, 4.5 µl of purified protein complexes were applied to glow
555 discharged Quantifoil 2/1 grids, blotted for 3.5 s with force 4 in a Vitrobot Mark III (Thermo
556 Fisher) at 100% humidity and 4°C, then plunge frozen in liquid ethane, cooled by liquid
557 nitrogen. Cryo-EM data was acquired with a FEI Titan Krios transmission electron microscope
558 using the SerialEM software¹⁰⁶. Movie frames were recorded at a nominal magnification of
559 22,500x using a K3 direct electron detector (Gatan), The total electron dose of ~55 electrons
560 per Å² was distributed over 30 frames at a calibrated physical pixel size of 1.09 Å. Micrographs
561 were recorded in a defocus range of -0.5 to -3.0 µm.

562 **Image processing, classification and refinement**

563 Cryo-EM micrographs were processed on the fly using the Focus software package¹⁰⁷ if they
564 passed the selection criteria (iciness < 1.05, drift 0.4 Å < x < 70 Å, defocus 0.5 µm < x < 5.5
565 µm, estimated CTF resolution < 6 Å). Micrograph frames were aligned using MotionCor2¹⁰⁸
566 and the contrast transfer function (CTF) for aligned frames was determined using Gctf¹⁰⁹. Using
567 Gautomatch (<http://www.mrc-lmb.cam.ac.uk/kzhang/>) 693,297 particles were picked template-
568 free on 824 acquired micrographs. Particles were extracted with a pixel box size of 260 using
569 RELION 3.1¹¹⁰ and imported into Cryosparc 2.3¹¹¹. After reference-free 2D classification,
570 675,123 particles were used for ab initio construction of initial models and subjected to multiple
571 rounds of 3D classification to obtain models with and without Psb28 density. Non-uniform

572 refinement in Cryosparc resulted in models with an estimated resolution of ~ 3.2 Å. Particles
573 belonging to 3D classes with and without Psb28 (150,090 and 166,411 particles, respectively)
574 were reextracted in RELION with a pixel box size of 256 and subjected to several rounds of
575 CTF-refinement (estimation of anisotropic magnification, fit of per-micrograph defocus and
576 astigmatism and beam tilt estimation) and Bayesian polishing¹¹². Both classes were refined
577 using the previously generated starting models. 3D classification without further alignment
578 using a mask around the Psb27 region separated particles in the Psb28-containing class into
579 distinct classes with and without Psb27 (57,862 and 91,473 particles, respectively). Final
580 refinement of each of the three classes (with Psb27 and Psb28 (PSII-I), with Psb28 but without
581 Psb27 (PSII-I'), and without Psb27 and Psb28 (PSII-M)) resulted in models with global
582 resolutions of 2.94 Å, 2.76 Å and 2.82 Å, respectively (Gold standard FSC analysis of two
583 independent half-sets at the 0.143 cutoff). Local-resolution and 3D-FSC plots (Extended Data
584 Fig. 2) were calculated using RELION and the “Remote 3DFSC Processing Server” web
585 interface¹¹³, respectively.

586 **Atomic model construction**

587 The 3.6 Å resolution X-ray structure of monomeric PSII from *T. elongatus* with PDB-ID 3KZI⁴⁴
588 was used as initial structural model that was docked as rigid body using Chimera¹¹⁴ into the
589 obtained cryo EM densities for PSII-M and PSII-I. The cofactors that had no corresponding
590 density were removed. The subunit PsbJ was also removed, as it was deleted in the experimental
591 design. By highlighting the still unoccupied parts of the PSII-I density map, we identified
592 densities that lead to the structures of Psb27, Psb28, and Psb34.

593 The 2.4 Å resolution X-ray structures of isolated Psb28 from *T. elongatus* with PDB-ID
594 3ZPN¹¹⁵ and the 1.6 Å resolution X-ray structure of isolated Psb27 from *T. elongatus* with
595 PDB-ID 2Y6X⁶⁰ were docked as rigid bodies into the unoccupied densities. The 1.6 Å
596 resolution X-ray structure of CyanoQ from *T. elongatus* with PDB-ID 3ZSU¹¹⁶ does not fit into
597 the density and was therefore not modeled.

598 As there was no experimentally resolved structural model of Psb34 available, we first used the
599 sequence with UniProt-ID Q8DMP8 to predict structures using the webserver SWISS Model¹¹⁷
600 and LOMETS¹¹⁸. We also predicted the secondary structure through the meta server
601 Bioinformatics Toolkit¹¹⁹ and CCTOP¹²⁰. The results of the secondary structure prediction are
602 summarized in Table S4. Combining these predictions together with the unassigned cryo-EM
603 density, we used COOT¹²¹ to build an initial model of Psb34 that has one α -helix from amino
604 acid number 28 to 55.

605 **Model Refinement**

606 The initial model of the complex described above was refined in real space against the cryo-
607 EM density of PSII-I, and structural clashes were removed using molecular dynamics flexible
608 fitting (MDFF)¹²². MDFF simulations were prepared in VMD 1.9.4a35¹²³ using QwikMD¹²⁴
609 and the MDFF plugin. The simulations were carried out with NAMD 2.13¹²⁵ employing the
610 CHARMM36 force field. Secondary structure, cis peptide and chirality restraints were
611 employed during 800 steps of minimization followed by a 40 ps MDFF simulation at 300K.
612 Due to the employed restraints, only conformational changes of side chains and subunit
613 movements compared to the initial structure are identified during the initial MDFF run. We
614 checked the fit to density of the structure by calculating cross-correlation values of the
615 backbone atoms. For PSII-I, we identified residues 217 to 269 from PsbA and residues 467 to
616 499 from PsbB and PsbZ as main regions where the structural model was not yet in accordance
617 with the density after the initial MDFF run. For these three regions, we employed an iterative
618 combination of MDFF with Rosetta^{126,127}. Here, we used the optimized strategy as described
619 for model construction of the 26S proteasome^{128,129}.

620 To obtain an atomic model that fit the PSII-M density, we used the initial model based on 3KZI
621 described above, but without PsbJ, Psb27, Psb28, and Psb34. After the initial MDFF run, the
622 cross-correlation check did not reveal any regions with significant deviation between model
623 and density. Therefore, no further refinement was necessary. This fast convergence reflects that
624 there are no crucial differences between the PSII-M model and the X-ray structure 3KZI.

625 To obtain the atomic model that fit the PSII-I' density, we used the final PSII-I model without
626 Psb27 for MDFF. After the initial MDFF run, the cross-correlation check did not reveal any
627 regions with significant deviation between model and density. This fast convergence reflects
628 that there are no crucial differences between the PSII-I and PSII-I' models, except for the
629 presence of the Psb27 subunit.

630 Last, the PSII-M, PSII-I, and PSII-I' models were used to initiate one final round of real-space
631 refinement in Phenix¹³⁰.

632 633 **Acknowledgements**

634 We thank C. König, M. Völkel, and R. Oworah-Nkruma for excellent technical assistance,
635 Kristin Becker for cloning of the pIVEX_{Psb28His} plasmid, Bibi Erjavec for preparation of the
636 scheme in Fig. 1 and Nicholas Cox for helpful discussion. J.M.S. is grateful to E. Conti for
637 scientific independence and great mentorship and to J. M. Plitzko and W. Baumeister for access
638 to the cryo-EM infrastructure and early career support. M.M.N. is grateful to his mentor M.

639 Rögner for generous support. **Funding:** Financial support was provided by the Max Planck
640 Society, the Helmholtz Zentrum München, the DFG research unit FOR2092 (EN 1194/1-1 to
641 B.D.E., NO 836/3-2 to M.M.N.), the DFG priority program 2002 (NO 836/4-1 to M.M.N.), the
642 grant NIH P41-GM104601 (to E.T.) and an Emmy-Noether fellowship (SCHU 3364/1-1 to
643 J.M.S). A.K.-L. was supported by the LabEx Saclay Plant Sciences-SPS (grant number ANR-
644 10-LABX-0040-SPS) and the French Infrastructure for Integrated Structural Biology (FRISBI;
645 grant number ANR-10-INSB-05). R.S. gratefully acknowledges support from the DFG (INST
646 213/757-1 FUGG and INST 213/843-1 FUGG). **Author contributions:** B.D.E., T.R., J.M.S.
647 and M.M.N. conceived the research, prepared the figures, and wrote the manuscript with the
648 contributions of all other authors. M.M.N. coordinated the activities. Preparation of mutants,
649 PSII isolation and biochemical analysis were performed by J.Z., M.M, P.L. and M.M.N. Mass
650 spectrometry analysis was done by J.M.-C. and J.D.L. J.M.S., S.B. and B.D.E. performed the
651 cryo-EM analysis and T.R. built the structural model with the help of S.K.S., A.C. and E.T.
652 Fluorescence spectroscopy was carried out by J.Z. and M.M.N. EPR experiments were
653 conducted by A.K.-L. NMR experiments were conducted and analyzed by O.A. and R.S.. All
654 authors approved the final version of the manuscript. **Competing interests:** The authors declare
655 no competing interests. **Data availability:** The cryo-EM density maps will be deposited in the
656 Electron Microscopy Data Bank, the atomic models of the cryo-EM structures in the worldwide
657 Protein Data Bank (wwPDB) and the NMR assignments for Psb28 in the Biological Magnetic
658 Resonance Bank (BMRB), respectively.

659 **References**

- 660 1 Hohmann-Marriott, M. F. & Blankenship, R. E. Evolution of photosynthesis. *Annual*
661 *review of plant biology* **62**, 515-548, doi:10.1146/annurev-arplant-042110-103811
662 (2011).
- 663 2 Sanchez-Baracaldo, P. & Cardona, T. On the origin of oxygenic photosynthesis and
664 Cyanobacteria. *New Phytol* **225**, 1440-1446, doi:10.1111/nph.16249 (2020).
- 665 3 Vinyard, D. J., Ananyev, G. M. & Dismukes, G. C. Photosystem II: the reaction center
666 of oxygenic photosynthesis. *Annual review of biochemistry* **82**, 577-606,
667 doi:10.1146/annurev-biochem-070511-100425 (2013).
- 668 4 Boekema, E. J. *et al.* Supramolecular structure of the photosystem II complex from
669 green plants and cyanobacteria. *Proc Natl Acad Sci U S A* **92**, 175-179,
670 doi:10.1073/pnas.92.1.175 (1995).
- 671 5 Cox, N., Pantazis, D. A. & Lubitz, W. Current Understanding of the Mechanism of
672 Water Oxidation in Photosystem II and Its Relation to XFEL Data. *Annual review of*
673 *biochemistry* **89**, 795-820, doi:10.1146/annurev-biochem-011520-104801 (2020).
- 674 6 Shen, J. R. The Structure of Photosystem II and the Mechanism of Water Oxidation in
675 Photosynthesis. *Annual review of plant biology* **66**, 23-48, doi:10.1146/annurev-arplant-
676 050312-120129 (2015).
- 677 7 Yano, J. *et al.* Light-dependent production of dioxygen in photosynthesis. *Met Ions Life*
678 *Sci* **15**, 13-43, doi:10.1007/978-3-319-12415-5_2 (2015).
- 679 8 Ferreira, K. N., Iverson, T. M., Maghlaoui, K., Barber, J. & Iwata, S. Architecture of
680 the photosynthetic oxygen-evolving center. *Science* **303**, 1831-1838,
681 doi:10.1126/science.1093087 (2004).
- 682 9 Cardona, T., Sedoud, A., Cox, N. & Rutherford, A. W. Charge separation in
683 photosystem II: a comparative and evolutionary overview. *Biochim Biophys Acta* **1817**,
684 26-43, doi:10.1016/j.bbabi.2011.07.012 (2012).
- 685 10 Holzwarth, A. R. *et al.* Kinetics and mechanism of electron transfer in intact
686 photosystem II and in the isolated reaction center: pheophytin is the primary electron
687 acceptor. *Proc Natl Acad Sci U S A* **103**, 6895-6900, doi:10.1073/pnas.0505371103
688 (2006).
- 689 11 Müh, F., Glöckner, C., Hellmich, J. & Zouni, A. Light-induced quinone reduction in
690 photosystem II. *Biochim Biophys Acta* **1817**, 44-65, doi:10.1016/j.bbabi.2011.05.021
691 (2012).
- 692 12 Faller, P. *et al.* Rapid formation of the stable tyrosyl radical in photosystem II. *Proc*
693 *Natl Acad Sci U S A* **98**, 14368-14373, doi:10.1073/pnas.251382598 (2001).
- 694 13 Roose, J. L., Frankel, L. K., Mummadisetti, M. P. & Bricker, T. M. The extrinsic
695 proteins of photosystem II: update. *Planta* **243**, 889-908, doi:10.1007/s00425-015-
696 2462-6 (2016).
- 697 14 Müh, F. & Zouni, A. Structural basis of light-harvesting in the photosystem II core
698 complex. *Protein Sci* **29**, 1090-1119, doi:10.1002/pro.3841 (2020).
- 699 15 Shi, L. X., Hall, M., Funk, C. & Schröder, W. P. Photosystem II, a growing complex:
700 updates on newly discovered components and low molecular mass proteins. *Biochim*
701 *Biophys Acta* **1817**, 13-25, doi:10.1016/j.bbabi.2011.08.008 (2012).
- 702 16 Stewart, D. H. & Brudvig, G. W. Cytochrome b559 of photosystem II. *Biochim Biophys*
703 *Acta* **1367**, 63-87, doi:10.1016/s0005-2728(98)00139-x (1998).
- 704 17 Cox, N. *et al.* Photosynthesis. Electronic structure of the oxygen-evolving complex in
705 photosystem II prior to O-O bond formation. *Science* **345**, 804-808,
706 doi:10.1126/science.1254910 (2014).
- 707 18 Kern, J. *et al.* Structures of the intermediates of Kok's photosynthetic water oxidation
708 clock. *Nature* **563**, 421-425, doi:10.1038/s41586-018-0681-2 (2018).

- 709 19 Kupitz, C. *et al.* Serial time-resolved crystallography of photosystem II using a
710 femtosecond X-ray laser. *Nature* **513**, 261-265, doi:10.1038/nature13453 (2014).
- 711 20 Suga, M. *et al.* An oxyl/oxo mechanism for oxygen-oxygen coupling in PSII revealed
712 by an x-ray free-electron laser. *Science* **366**, 334-338, doi:10.1126/science.aax6998
713 (2019).
- 714 21 Umena, Y., Kawakami, K., Shen, J. R. & Kamiya, N. Crystal structure of oxygen-
715 evolving photosystem II at a resolution of 1.9 Å. *Nature* **473**, 55-60,
716 doi:10.1038/nature09913 (2011).
- 717 22 Krieger-Liszczay, A., Fufezan, C. & Trebst, A. Singlet oxygen production in
718 photosystem II and related protection mechanism. *Photosynth Res* **98**, 551-564,
719 doi:10.1007/s11120-008-9349-3 (2008).
- 720 23 Vass, I. Molecular mechanisms of photodamage in the Photosystem II complex.
721 *Biochim Biophys Acta* **1817**, 209-217, doi:10.1016/j.bbabi.2011.04.014 (2012).
- 722 24 Heinz, S., Liauw, P., Nickelsen, J. & Nowaczyk, M. Analysis of photosystem II
723 biogenesis in cyanobacteria. *Biochim Biophys Acta* **1857**, 274-287,
724 doi:10.1016/j.bbabi.2015.11.007 (2016).
- 725 25 Nickelsen, J. & Rengstl, B. Photosystem II assembly: from cyanobacteria to plants.
726 *Annual review of plant biology* **64**, 609-635, doi:10.1146/annurev-arplant-050312-
727 120124 (2013).
- 728 26 Nixon, P. J., Michoux, F., Yu, J., Boehm, M. & Komenda, J. Recent advances in
729 understanding the assembly and repair of photosystem II. *Ann Bot* **106**, 1-16,
730 doi:10.1093/aob/mcq059 (2010).
- 731 27 Komenda, J. *et al.* Cleavage after residue Ala352 in the C-terminal extension is an early
732 step in the maturation of the D1 subunit of Photosystem II in *Synechocystis* PCC 6803.
733 *Biochim Biophys Acta* **1767**, 829-837, doi:10.1016/j.bbabi.2007.01.005 (2007).
- 734 28 Komenda, J. *et al.* The cyanobacterial homologue of HCF136/YCF48 is a component
735 of an early photosystem II assembly complex and is important for both the efficient
736 assembly and repair of photosystem II in *Synechocystis* sp. PCC 6803. *J Biol Chem* **283**,
737 22390-22399, doi:10.1074/jbc.M801917200 (2008).
- 738 29 Boehm, M. *et al.* Subunit composition of CP43-less photosystem II complexes of
739 *Synechocystis* sp. PCC 6803: implications for the assembly and repair of photosystem
740 II. *Philos Trans R Soc Lond B Biol Sci* **367**, 3444-3454, doi:10.1098/rstb.2012.0066
741 (2012).
- 742 30 Dobáková, M., Sobotka, R., Tichy, M. & Komenda, J. Psb28 protein is involved in the
743 biogenesis of the photosystem II inner antenna CP47 (PsbB) in the cyanobacterium
744 *Synechocystis* sp. PCC 6803. *Plant Physiol* **149**, 1076-1086,
745 doi:10.1104/pp.108.130039 (2009).
- 746 31 Komenda, J. *et al.* The Psb27 assembly factor binds to the CP43 complex of
747 photosystem II in the cyanobacterium *Synechocystis* sp. PCC 6803. *Plant Physiol* **158**,
748 476-486, doi:10.1104/pp.111.184184 (2012).
- 749 32 Mamedov, F., Nowaczyk, M. M., Thapper, A., Rögner, M. & Styring, S. Functional
750 characterization of monomeric photosystem II core preparations from
751 *Thermosynechococcus elongatus* with or without the Psb27 protein. *Biochemistry* **46**,
752 5542-5551, doi:10.1021/bi7000399 (2007).
- 753 33 Nowaczyk, M. M. *et al.* Psb27, a cyanobacterial lipoprotein, is involved in the repair
754 cycle of photosystem II. *Plant Cell* **18**, 3121-3131, doi:10.1105/tpc.106.042671 (2006).
- 755 34 Roose, J. L. & Pakrasi, H. B. The Psb27 protein facilitates manganese cluster assembly
756 in photosystem II. *J Biol Chem* **283**, 4044-4050, doi:10.1074/jbc.M708960200 (2008).
- 757 35 Nowaczyk, M. M. *et al.* Deletion of *psbJ* leads to accumulation of Psb27-Psb28
758 photosystem II complexes in *Thermosynechococcus elongatus*. *Biochim Biophys Acta*
759 **1817**, 1339-1345, doi:10.1016/j.bbabi.2012.02.017 (2012).

- 760 36 Sakata, S., Mizusawa, N., Kubota-Kawai, H., Sakurai, I. & Wada, H. Psb28 is involved
761 in recovery of photosystem II at high temperature in *Synechocystis* sp. PCC 6803.
762 *Biochim Biophys Acta* **1827**, 50-59, doi:10.1016/j.bbabbio.2012.10.004 (2013).
- 763 37 Weisz, D. A. *et al.* Mass spectrometry-based cross-linking study shows that the Psb28
764 protein binds to cytochrome b559 in Photosystem II. *Proc Natl Acad Sci U S A* **114**,
765 2224-2229, doi:10.1073/pnas.1620360114 (2017).
- 766 38 Bečková, M. *et al.* Association of Psb28 and Psb27 Proteins with PSII-PSI
767 Supercomplexes upon Exposure of *Synechocystis* sp. PCC 6803 to High Light. *Mol*
768 *Plant* **10**, 62-72, doi:10.1016/j.molp.2016.08.001 (2017).
- 769 39 Bentley, F. K., Luo, H., Dilbeck, P., Burnap, R. L. & Eaton-Rye, J. J. Effects of
770 inactivating psbM and psbT on photodamage and assembly of photosystem II in
771 *Synechocystis* sp. PCC 6803. *Biochemistry* **47**, 11637-11646, doi:10.1021/bi800804h
772 (2008).
- 773 40 Grasse, N. *et al.* Role of novel dimeric Photosystem II (PSII)-Psb27 protein complex in
774 PSII repair. *J Biol Chem* **286**, 29548-29555, doi:10.1074/jbc.M111.238394 (2011).
- 775 41 Liu, H., Roose, J. L., Cameron, J. C. & Pakrasi, H. B. A genetically tagged Psb27 protein
776 allows purification of two consecutive photosystem II (PSII) assembly intermediates in
777 *Synechocystis* 6803, a cyanobacterium. *J Biol Chem* **286**, 24865-24871,
778 doi:10.1074/jbc.M111.246231 (2011).
- 779 42 Weisz, D. A. *et al.* A novel chlorophyll protein complex in the repair cycle of
780 photosystem II. *Proc Natl Acad Sci U S A* **116**, 21907-21913,
781 doi:10.1073/pnas.1909644116 (2019).
- 782 43 Mabbitt, P. D., Wilbanks, S. M. & Eaton-Rye, J. J. Structure and function of the
783 hydrophilic Photosystem II assembly proteins: Psb27, Psb28 and Ycf48. *Plant Physiol*
784 *Biochem* **81**, 96-107, doi:10.1016/j.plaphy.2014.02.013 (2014).
- 785 44 Broser, M. *et al.* Crystal structure of monomeric photosystem II from
786 *Thermosynechococcus elongatus* at 3.6-Å resolution. *J Biol Chem* **285**, 26255-26262,
787 doi:10.1074/jbc.M110.127589 (2010).
- 788 45 Komenda, J. & Sobotka, R. Cyanobacterial high-light-inducible proteins--Protectors of
789 chlorophyll-protein synthesis and assembly. *Biochim Biophys Acta* **1857**, 288-295,
790 doi:10.1016/j.bbabbio.2015.08.011 (2016).
- 791 46 Mulo, P. *et al.* Mutagenesis of the D-E loop of photosystem II reaction centre protein
792 D1. Function and assembly of photosystem II. *Plant Mol Biol* **33**, 1059-1071,
793 doi:10.1023/a:1005765305956 (1997).
- 794 47 Eaton-Rye, J. J. & Govindjee. Electron transfer through the quinone acceptor complex
795 of photosystem II in bicarbonate-depleted spinach thylakoid membranes as a function
796 of actinic flash number and frequency. *Biochimica et Biophysica Acta (BBA)-*
797 *Bioenergetics* **935**, 237-247 (1988).
- 798 48 Allen, J. F. & Nield, J. Redox Tuning in Photosystem II. *Trends Plant Sci* **22**, 97-99,
799 doi:10.1016/j.tplants.2016.11.011 (2017).
- 800 49 Brinkert, K., De Causmaecker, S., Krieger-Liszkay, A., Fantuzzi, A. & Rutherford, A.
801 W. Bicarbonate-induced redox tuning in Photosystem II for regulation and protection.
802 *Proc Natl Acad Sci U S A* **113**, 12144-12149, doi:10.1073/pnas.1608862113 (2016).
- 803 50 Vass, I., Kirilovsky, D. & Etienne, A. L. UV-B radiation-induced donor- and acceptor-
804 side modifications of photosystem II in the cyanobacterium *Synechocystis* sp. PCC
805 6803. *Biochemistry* **38**, 12786-12794, doi:10.1021/bi991094w (1999).
- 806 51 Johnson, G. N., Rutherford, A. W. & Krieger, A. A change in the midpoint potential of
807 the quinone QA in photosystem II associated with photoactivation of oxygen evolution.
808 *Biochim Biophys Acta* **1229**, 202-207 (1995).

809 52 Johnson, G. N., Boussac, A. & Rutherford, A. W. The origin of 40–50 C
810 thermoluminescence bands in photosystem II. *Biochim Biophys Acta* **1184**, 85-92
811 (1994).

812 53 Stowell, M. H. *et al.* Light-induced structural changes in photosynthetic reaction center:
813 implications for mechanism of electron-proton transfer. *Science* **276**, 812-816,
814 doi:10.1126/science.276.5313.812 (1997).

815 54 Cormann, K. U., Möller, M. & Nowaczyk, M. M. Critical Assessment of Protein Cross-
816 Linking and Molecular Docking: An Updated Model for the Interaction Between
817 Photosystem II and Psb27. *Front Plant Sci* **7**, 157, doi:10.3389/fpls.2016.00157 (2016).

818 55 Liu, H., Huang, R. Y., Chen, J., Gross, M. L. & Pakrasi, H. B. Psb27, a transiently
819 associated protein, binds to the chlorophyll binding protein CP43 in photosystem II
820 assembly intermediates. *Proc Natl Acad Sci U S A* **108**, 18536-18541,
821 doi:10.1073/pnas.1111597108 (2011).

822 56 Wei, X. *et al.* Structure of spinach photosystem II-LHCII supercomplex at 3.2 Å
823 resolution. *Nature* **534**, 69-74, doi:10.1038/nature18020 (2016).

824 57 Cormann, K. U. *et al.* Structure of Psb27 in solution: implications for transient binding
825 to photosystem II during biogenesis and repair. *Biochemistry* **48**, 8768-8770,
826 doi:10.1021/bi9012726 (2009).

827 58 Fagerlund, R. D. & Eaton-Rye, J. J. The lipoproteins of cyanobacterial photosystem II.
828 *J Photochem Photobiol B* **104**, 191-203, doi:10.1016/j.jphotobiol.2011.01.022 (2011).

829 59 Liu, H. *et al.* Mass spectrometry-based footprinting reveals structural dynamics of loop
830 E of the chlorophyll-binding protein CP43 during photosystem II assembly in the
831 cyanobacterium *Synechocystis* 6803. *J Biol Chem* **288**, 14212-14220,
832 doi:10.1074/jbc.M113.467613 (2013).

833 60 Michoux, F. *et al.* Crystal structure of the Psb27 assembly factor at 1.6 Å: implications
834 for binding to Photosystem II. *Photosynth Res* **110**, 169-175, doi:10.1007/s11120-011-
835 9712-7 (2012).

836 61 Weisz, D. A., Gross, M. L. & Pakrasi, H. B. The Use of Advanced Mass Spectrometry
837 to Dissect the Life-Cycle of Photosystem II. *Front Plant Sci* **7**, 617,
838 doi:10.3389/fpls.2016.00617 (2016).

839 62 Kettunen, R., Tyystjarvi, E. & Aro, E. M. Degradation pattern of photosystem II
840 reaction center protein D1 in intact leaves. The major photoinhibition-induced cleavage
841 site in D1 polypeptide is located amino terminally of the DE loop. *Plant Physiol* **111**,
842 1183-1190, doi:10.1104/pp.111.4.1183 (1996).

843 63 Mulo, P., Laakso, S., Maenpaa, P. & Aro, E. M. Stepwise photoinhibition of
844 photosystem II. Studies with *Synechocystis* species PCC 6803 mutants with a modified
845 D-E loop of the reaction center polypeptide D1. *Plant Physiol* **117**, 483-490,
846 doi:10.1104/pp.117.2.483 (1998).

847 64 Wang, X. *et al.* Is bicarbonate in Photosystem II the equivalent of the glutamate ligand
848 to the iron atom in bacterial reaction centers? *Biochim Biophys Acta* **1100**, 1-8,
849 doi:10.1016/0005-2728(92)90119-m (1992).

850 65 Cheap, H. *et al.* M234Glu is a component of the proton sponge in the reaction center
851 from photosynthetic bacteria. *Biochim Biophys Acta* **1787**, 1505-1515,
852 doi:10.1016/j.bbabi.2009.07.004 (2009).

853 66 Bao, H. & Burnap, R. L. Photoactivation: The Light-Driven Assembly of the Water
854 Oxidation Complex of Photosystem II. *Front Plant Sci* **7**, 578,
855 doi:10.3389/fpls.2016.00578 (2016).

856 67 Becker, K., Cormann, K. U. & Nowaczyk, M. M. Assembly of the water-oxidizing
857 complex in photosystem II. *J Photochem Photobiol B* **104**, 204-211,
858 doi:10.1016/j.jphotobiol.2011.02.005 (2011).

- 859 68 Cheniae, G. & Martin, I. Photoactivation of the manganese catalyst of O₂ evolution. I-
860 Biochemical and kinetic aspects. *Biochim Biophys Acta* **253**, 167-181,
861 doi:10.1016/0005-2728(71)90242-8 (1971).
- 862 69 Dasgupta, J., Ananyev, G. M. & Dismukes, G. C. Photoassembly of the Water-
863 Oxidizing Complex in Photosystem II. *Coord Chem Rev* **252**, 347-360,
864 doi:10.1016/j.ccr.2007.08.022 (2008).
- 865 70 Zhang, M. *et al.* Structural insights into the light-driven auto-assembly process of the
866 water-oxidizing Mn₄CaO₅-cluster in photosystem II. *Elife* **6**, doi:10.7554/eLife.26933
867 (2017).
- 868 71 Gisriel, C. J. *et al.* Cryo-EM Structure of Monomeric Photosystem II from
869 *Synechocystis* sp. PCC 6803 Lacking the Water-Oxidation Complex. *Joule* (2020).
- 870 72 Kolling, D. R., Cox, N., Ananyev, G. M., Pace, R. J. & Dismukes, G. C. What are the
871 oxidation states of manganese required to catalyze photosynthetic water oxidation?
872 *Biophys J* **103**, 313-322, doi:10.1016/j.bpj.2012.05.031 (2012).
- 873 73 Zaltsman, L., Ananyev, G. M., Bruntrager, E. & Dismukes, G. C. Quantitative kinetic
874 model for photoassembly of the photosynthetic water oxidase from its inorganic
875 constituents: requirements for manganese and calcium in the kinetically resolved steps.
876 *Biochemistry* **36**, 8914-8922, doi:10.1021/bi970187f (1997).
- 877 74 Nixon, P. J. & Diner, B. A. Aspartate 170 of the photosystem II reaction center
878 polypeptide D1 is involved in the assembly of the oxygen-evolving manganese cluster.
879 *Biochemistry* **31**, 942-948, doi:10.1021/bi00118a041 (1992).
- 880 75 Tyryshkin, A. M. *et al.* Spectroscopic evidence for Ca²⁺ involvement in the assembly
881 of the Mn₄Ca cluster in the photosynthetic water-oxidizing complex. *Biochemistry* **45**,
882 12876-12889, doi:10.1021/bi061495t (2006).
- 883 76 Campbell, K. A. *et al.* Dual-mode EPR detects the initial intermediate in photoassembly
884 of the photosystem II Mn cluster: the influence of amino acid residue 170 of the D1
885 polypeptide on Mn coordination. *Journal of the American Chemical Society* **122**, 3754-
886 3761 (2000).
- 887 77 Cohen, R. O., Nixon, P. J. & Diner, B. A. Participation of the C-terminal region of the
888 D1-polypeptide in the first steps in the assembly of the Mn₄Ca cluster of photosystem
889 II. *J Biol Chem* **282**, 7209-7218, doi:10.1074/jbc.M606255200 (2007).
- 890 78 Kuhl, H. *et al.* Towards structural determination of the water-splitting enzyme.
891 Purification, crystallization, and preliminary crystallographic studies of photosystem II
892 from a thermophilic cyanobacterium. *J Biol Chem* **275**, 20652-20659,
893 doi:10.1074/jbc.M001321200 (2000).
- 894 79 Iwai, M., Katoh, H., Katayama, M. & Ikeuchi, M. Improved genetic transformation of
895 the thermophilic cyanobacterium, *Thermosynechococcus elongatus* BP-1. *Plant Cell*
896 *Physiol* **45**, 171-175, doi:10.1093/pcp/pch015 (2004).
- 897 80 Cormann, K. U., Bartsch, M., Rögner, M. & Nowaczyk, M. M. Localization of the
898 CyanoP binding site on photosystem II by surface plasmon resonance spectroscopy.
899 *Front Plant Sci* **5**, 595, doi:10.3389/fpls.2014.00595 (2014).
- 900 81 Studier, F. W. Protein production by auto-induction in high density shaking cultures.
901 *Protein Expr Purif* **41**, 207-234, doi:10.1016/j.pep.2005.01.016 (2005).
- 902 82 Neff, D. & Dencher, N. A. Purification of multisubunit membrane protein complexes:
903 isolation of chloroplast FoF₁-ATP synthase, CF_o and CF₁ by blue native
904 electrophoresis. *Biochem Biophys Res Commun* **259**, 569-575,
905 doi:10.1006/bbrc.1999.0820 (1999).
- 906 83 Schagger, H. & von Jagow, G. Tricine-sodium dodecyl sulfate-polyacrylamide gel
907 electrophoresis for the separation of proteins in the range from 1 to 100 kDa. *Anal*
908 *Biochem* **166**, 368-379, doi:10.1016/0003-2697(87)90587-2 (1987).

- 909 84 Grzesiek, S. & Bax, A. Improved 3D triple-resonance NMR techniques applied to a 31
910 kDa protein. *Journal of Magnetic Resonance (1969)* **96**, 432-440 (1992).
- 911 85 Schleucher, J., Sattler, M. & Griesinger, C. Coherence selection by gradients without
912 signal attenuation: application to the three-dimensional HNC0 experiment. *Angew*
913 *Chem Int Ed Engl* **32**, 1489-1491 (1993).
- 914 86 Grzesiek, S. & Bax, A. Amino acid type determination in the sequential assignment
915 procedure of uniformly ¹³C/¹⁵N-enriched proteins. *J Biomol NMR* **3**, 185-204,
916 doi:10.1007/BF00178261 (1993).
- 917 87 Vuister, G. W. & Bax, A. Quantitative J correlation: a new approach for measuring
918 homonuclear three-bond J (HNH. alpha.) coupling constants in ¹⁵N-enriched proteins.
919 *J. Am. Chem. Soc.* **115**, 7772-7777 (1993).
- 920 88 Kay, L. E., Xu, G.-Y., Singer, A. U., Muhandiram, D. R. & Forman-Kay, J. D. A
921 gradient-enhanced HCCH-TOCSY experiment for recording side-chain ¹H and ¹³C
922 correlations in H₂O samples for proteins. *Journal of magnetic resonance. Series B* **101**,
923 333-337 (1993).
- 924 89 Sattler, M., Schwalbe, H. & Griesinger, C. Stereospecific assignment of leucine methyl
925 groups with carbon-13 in natural abundance or with random ¹³C labeling. *J Am Chem*
926 *Soc* **114**, 1126-1127 (1992).
- 927 90 Davis, J. H. Refocusing revisited: an optimized, gradient-enhanced refocused HSQC
928 and its applications in 2D and 3D NMR and in deuterium exchange experiments. *J*
929 *Biomol NMR* **5**, 433-437, doi:10.1007/BF00182288 (1995).
- 930 91 Davis, A. L., Keeler, J., Laue, E. D. & Moskau, D. Experiments for recording pure-
931 absorption heteronuclear correlation spectra using pulsed field gradients. *Journal of*
932 *Magnetic Resonance* **98**, 207-216 (1992).
- 933 92 Delaglio, F. *et al.* NMRPipe: a multidimensional spectral processing system based on
934 UNIX pipes. *J Biomol NMR* **6**, 277-293, doi:10.1007/BF00197809 (1995).
- 935 93 Vranken, W. F. *et al.* The CCPN data model for NMR spectroscopy: development of a
936 software pipeline. *Proteins* **59**, 687-696, doi:10.1002/prot.20449 (2005).
- 937 94 Yamazaki, T., Lee, W., Arrowsmith, C. H., Muhandiram, D. R. & Kay, L. E. A suite of
938 triple resonance NMR experiments for the backbone assignment of ¹⁵N, ¹³C, ²H
939 labeled proteins with high sensitivity. *J. Am. Chem. Soc.* **116**, 11655-11666 (1994).
- 940 95 Muhandiram, D., Xu, G. Y. & Kay, L. E. An enhanced-sensitivity pure absorption
941 gradient 4D ¹⁵N, ¹³C-edited NOESY experiment. *Journal of Biomolecular NMR* **3**,
942 463-470 (1993).
- 943 96 Wittekind, M. & Mueller, L. HNCACB, a high-sensitivity 3D NMR experiment to
944 correlate amide-proton and nitrogen resonances with the alpha- and beta-carbon
945 resonances in proteins. *Journal of magnetic resonance. Series B* **101**, 201-205 (1993).
- 946 97 Clubb, R., Thanabal, V. & Wagner, G. Constant time 3-dimensional triple resonance
947 pulse scheme to intraresidue H-1 (N), N-15, C-13' chemical shifts in N-15, C-13
948 enriched proteins. *J. Magn. Reson* **97**, 213-217 (1992).
- 949 98 Logan, T. M., Olejniczak, E. T., Xu, R. X. & Fesik, S. W. A general method for
950 assigning NMR spectra of denatured proteins using 3D HC(CO)NH-TOCSY triple
951 resonance experiments. *J Biomol NMR* **3**, 225-231, doi:10.1007/BF00178264 (1993).
- 952 99 Lyons, B. & Montelione, G. An HCCNH triple-resonance experiment using carbon-13
953 isotropic mixing for correlating backbone amide and side-chain aliphatic resonances in
954 isotopically enriched proteins. *Journal of magnetic resonance. Series B (Print)* **101**,
955 206-209 (1993).
- 956 100 Barbato, G., Ikura, M., Kay, L. E., Pastor, R. W. & Bax, A. Backbone dynamics of
957 calmodulin studied by ¹⁵N relaxation using inverse detected two-dimensional NMR
958 spectroscopy: the central helix is flexible. *Biochemistry* **31**, 5269-5278,
959 doi:10.1021/bi00138a005 (1992).

960 101 Ross, A., Czisch, M., Zinc, T. & Holak, T. A. Improved spectral quality in
961 measurements of heteronuclear NOE enhancement in proteins in water using pulsed
962 field gradients. *Journal of magnetic resonance. Series B (Print)* **102**, 314-316 (1993).

963 102 Mori, S., Abeygunawardana, C., Johnson, M. O. & van Zijl, P. C. Improved sensitivity
964 of HSQC spectra of exchanging protons at short interscan delays using a new fast HSQC
965 (FHSQC) detection scheme that avoids water saturation. *J Magn Reson B* **108**, 94-98,
966 doi:10.1006/jmrb.1995.1109 (1995).

967 103 Waudby, C. A., Ramos, A., Cabrita, L. D. & Christodoulou, J. Two-Dimensional NMR
968 Lineshape Analysis. *Sci Rep* **6**, 24826, doi:10.1038/srep24826 (2016).

969 104 Shen, J. R. & Inoue, Y. Binding and functional properties of two new extrinsic
970 components, cytochrome c-550 and a 12-kDa protein, in cyanobacterial photosystem II.
971 *Biochemistry* **32**, 1825-1832, doi:10.1021/bi00058a017 (1993).

972 105 Hideg, É. *et al.* Pure forms of the singlet oxygen sensors TEMP and TEMPD do not
973 inhibit Photosystem II. *Biochim Biophys Acta* **1807**, 1658-1661 (2011).

974 106 Mastronarde, D. N. Automated electron microscope tomography using robust prediction
975 of specimen movements. *Journal of structural biology* **152**, 36-51 (2005).

976 107 Biyani, N. *et al.* Focus: The interface between data collection and data processing in
977 cryo-EM. *J Struct Biol* **198**, 124-133, doi:10.1016/j.jsb.2017.03.007 (2017).

978 108 Zheng, S. Q. *et al.* MotionCor2: anisotropic correction of beam-induced motion for
979 improved cryo-electron microscopy. *Nat Methods* **14**, 331-332,
980 doi:10.1038/nmeth.4193 (2017).

981 109 Zhang, K. Gctf: Real-time CTF determination and correction. *J Struct Biol* **193**, 1-12,
982 doi:10.1016/j.jsb.2015.11.003 (2016).

983 110 Scheres, S. H. A Bayesian view on cryo-EM structure determination. *J Mol Biol* **415**,
984 406-418, doi:10.1016/j.jmb.2011.11.010 (2012).

985 111 Punjani, A., Rubinstein, J. L., Fleet, D. J. & Brubaker, M. A. cryoSPARC: algorithms
986 for rapid unsupervised cryo-EM structure determination. *Nat Methods* **14**, 290-296,
987 doi:10.1038/nmeth.4169 (2017).

988 112 Scheres, S. H. Beam-induced motion correction for sub-megadalton cryo-EM particles.
989 *Elife* **3**, e03665, doi:10.7554/eLife.03665 (2014).

990 113 Tan, Y. Z. *et al.* Addressing preferred specimen orientation in single-particle cryo-EM
991 through tilting. *Nat Methods* **14**, 793-796, doi:10.1038/nmeth.4347 (2017).

992 114 Pettersen, E. F. *et al.* UCSF Chimera--a visualization system for exploratory research
993 and analysis. *J Comput Chem* **25**, 1605-1612, doi:10.1002/jcc.20084 (2004).

994 115 Bialek, W. *et al.* Crystal structure of the Psb28 accessory factor of
995 *Thermosynechococcus elongatus* photosystem II at 2.3 Å. *Photosynth Res* **117**, 375-
996 383, doi:10.1007/s11120-013-9939-6 (2013).

997 116 Michoux, F. *et al.* Crystal structure of CyanoQ from the thermophilic cyanobacterium
998 *Thermosynechococcus elongatus* and detection in isolated photosystem II complexes.
999 *Photosynth Res* **122**, 57-67, doi:10.1007/s11120-014-0010-z (2014).

1000 117 Schwede, T., Kopp, J., Guex, N. & Peitsch, M. C. SWISS-MODEL: An automated
1001 protein homology-modeling server. *Nucleic Acids Res* **31**, 3381-3385,
1002 doi:10.1093/nar/gkg520 (2003).

1003 118 Wu, S. & Zhang, Y. LOMETS: a local meta-threading-server for protein structure
1004 prediction. *Nucleic Acids Res* **35**, 3375-3382, doi:10.1093/nar/gkm251 (2007).

1005 119 Zimmermann, L. *et al.* A Completely Reimplemented MPI Bioinformatics Toolkit with
1006 a New HHpred Server at its Core. *J Mol Biol* **430**, 2237-2243,
1007 doi:10.1016/j.jmb.2017.12.007 (2018).

1008 120 Dobson, L., Remenyi, I. & Tusnady, G. E. CCTOP: a Consensus Constrained TOPology
1009 prediction web server. *Nucleic Acids Res* **43**, W408-412, doi:10.1093/nar/gkv451
1010 (2015).

- 1011 121 Emsley, P., Lohkamp, B., Scott, W. G. & Cowtan, K. Features and development of
1012 Coot. *Acta Crystallogr D Biol Crystallogr* **66**, 486-501,
1013 doi:10.1107/S0907444910007493 (2010).
- 1014 122 Trabuco, L. G., Villa, E., Schreiner, E., Harrison, C. B. & Schulten, K. Molecular
1015 dynamics flexible fitting: a practical guide to combine cryo-electron microscopy and X-
1016 ray crystallography. *Methods* **49**, 174-180, doi:10.1016/j.ymeth.2009.04.005 (2009).
- 1017 123 Humphrey, W., Dalke, A. & Schulten, K. VMD: visual molecular dynamics. *J Mol*
1018 *Graph* **14**, 33-38, doi:10.1016/0263-7855(96)00018-5 (1996).
- 1019 124 Ribeiro, J. V. *et al.* QwikMD - Integrative Molecular Dynamics Toolkit for Novices and
1020 Experts. *Sci Rep* **6**, 26536, doi:10.1038/srep26536 (2016).
- 1021 125 Phillips, J. C. *et al.* Scalable molecular dynamics with NAMD. *J Comput Chem* **26**,
1022 1781-1802, doi:10.1002/jcc.20289 (2005).
- 1023 126 Leaver-Fay, A. *et al.* ROSETTA3: an object-oriented software suite for the simulation
1024 and design of macromolecules. *Methods Enzymol* **487**, 545-574, doi:10.1016/B978-0-
1025 12-381270-4.00019-6 (2011).
- 1026 127 Lindert, S. & McCammon, J. A. Improved cryoEM-Guided Iterative Molecular
1027 Dynamics--Rosetta Protein Structure Refinement Protocol for High Precision Protein
1028 Structure Prediction. *J Chem Theory Comput* **11**, 1337-1346, doi:10.1021/ct500995d
1029 (2015).
- 1030 128 Guo, Q. *et al.* In Situ Structure of Neuronal C9orf72 Poly-GA Aggregates Reveals
1031 Proteasome Recruitment. *Cell* **172**, 696-705 e612, doi:10.1016/j.cell.2017.12.030
1032 (2018).
- 1033 129 Wehmer, M. *et al.* Structural insights into the functional cycle of the ATPase module of
1034 the 26S proteasome. *Proc Natl Acad Sci U S A* **114**, 1305-1310,
1035 doi:10.1073/pnas.1621129114 (2017).
- 1036 130 Liebschner, D. *et al.* Macromolecular structure determination using X-rays, neutrons
1037 and electrons: recent developments in Phenix. *Acta Crystallogr D Struct Biol* **75**, 861-
1038 877, doi:10.1107/S2059798319011471 (2019).

Figures

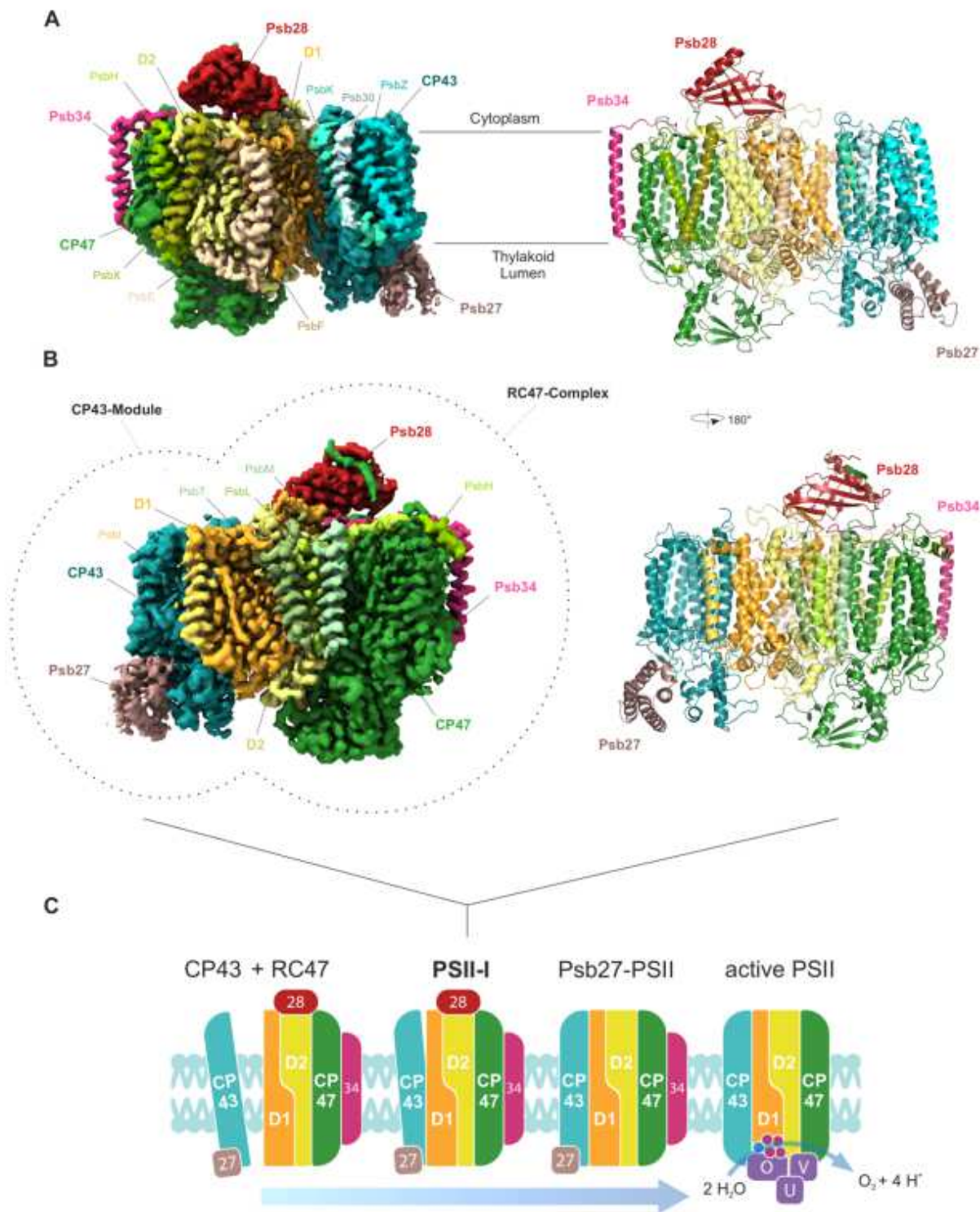


Figure 1

Cryo-EM map of a PSII assembly intermediate (PSII-I) from *T. elongatus*, segmented by subunit. (A) 15 PSII subunits and 3 assembly factors are colored and named (PSII subunits: D1, D2, CP43, CP47, PsbE, PsbF, PsbH, PsbI, PsbK, PsbL, PsbM, PsbT, PsbX, PsbZ and Psb30; assembly factors: Psb27, Psb28 and

tsl0063, which we named Psb34) (front view). (B) Parts of PSII that originate from the CP43 module (comprised of CP43, Psb27, PsbZ, Psb30 and PsbK) and the RC47 complex are indicated by dashed lines (back view). Schematic model of the PSII assembly process starting with the formation of PSII-I from the CP43 module and RC47. Small PSII subunits were omitted for simplicity.

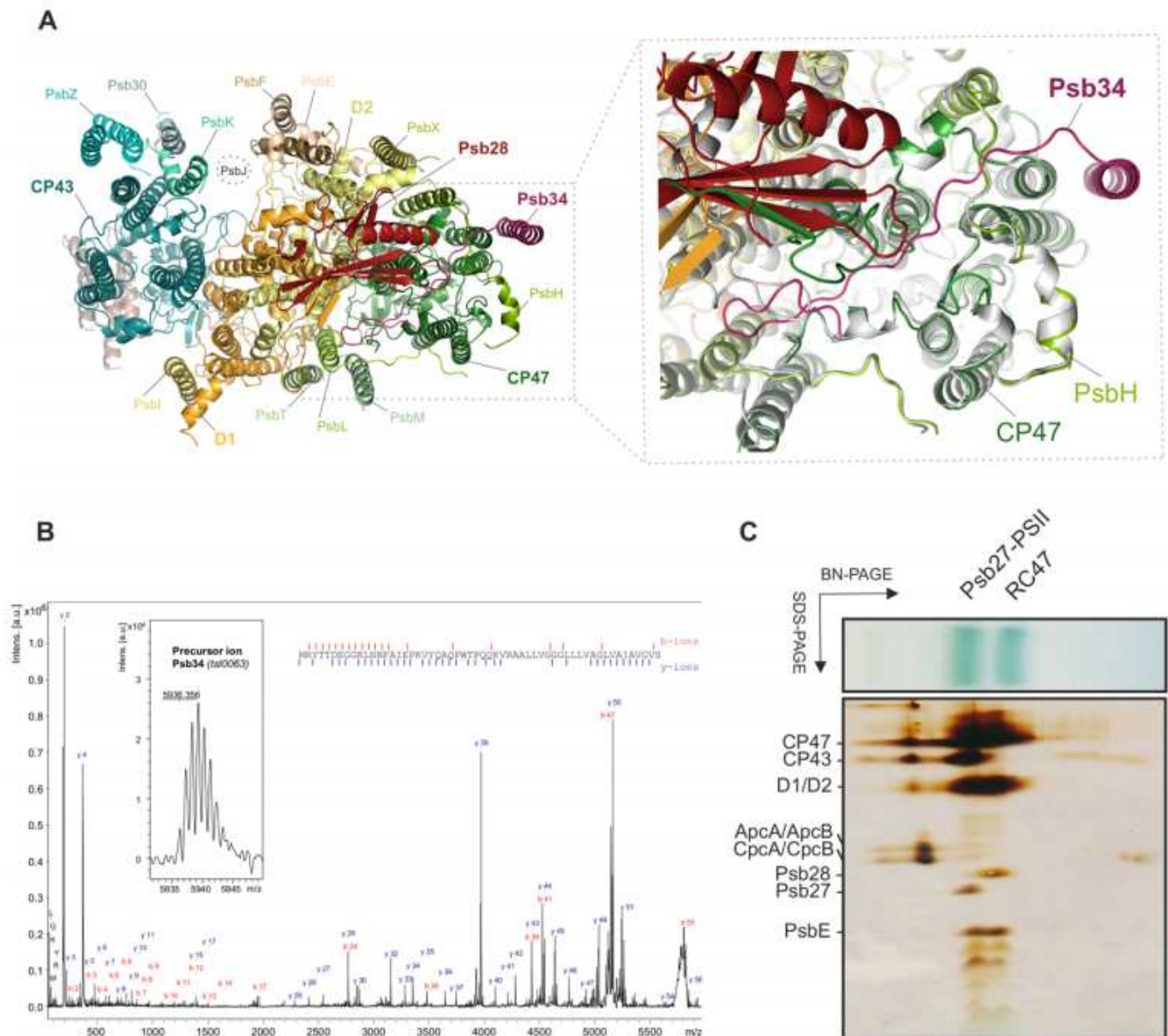


Figure 2

Psb34 binds to RC47 during attachment of the CP43 module. (A) Binding site of Psb34 at CP47, close to PsbH (top view), with extended binding of the Psb34 N-terminus along the cytoplasmic PSII surface (dashed box). (B) MALDI-ToF analysis of PSII assembly intermediates. Mass spectrum of Psb34 (tsl0063) from the PSII complex (inset) and the fragment spectrum obtained for m/z 5936.356 with annotated b- and y-ion series matching the Psb34 sequence. Observed fragmentation sites are indicated

by dashes in the sequence. Mascot score: 171. (C) Subunit composition of Psb34-PSII assembly intermediates analyzed by 2D-PAGE.

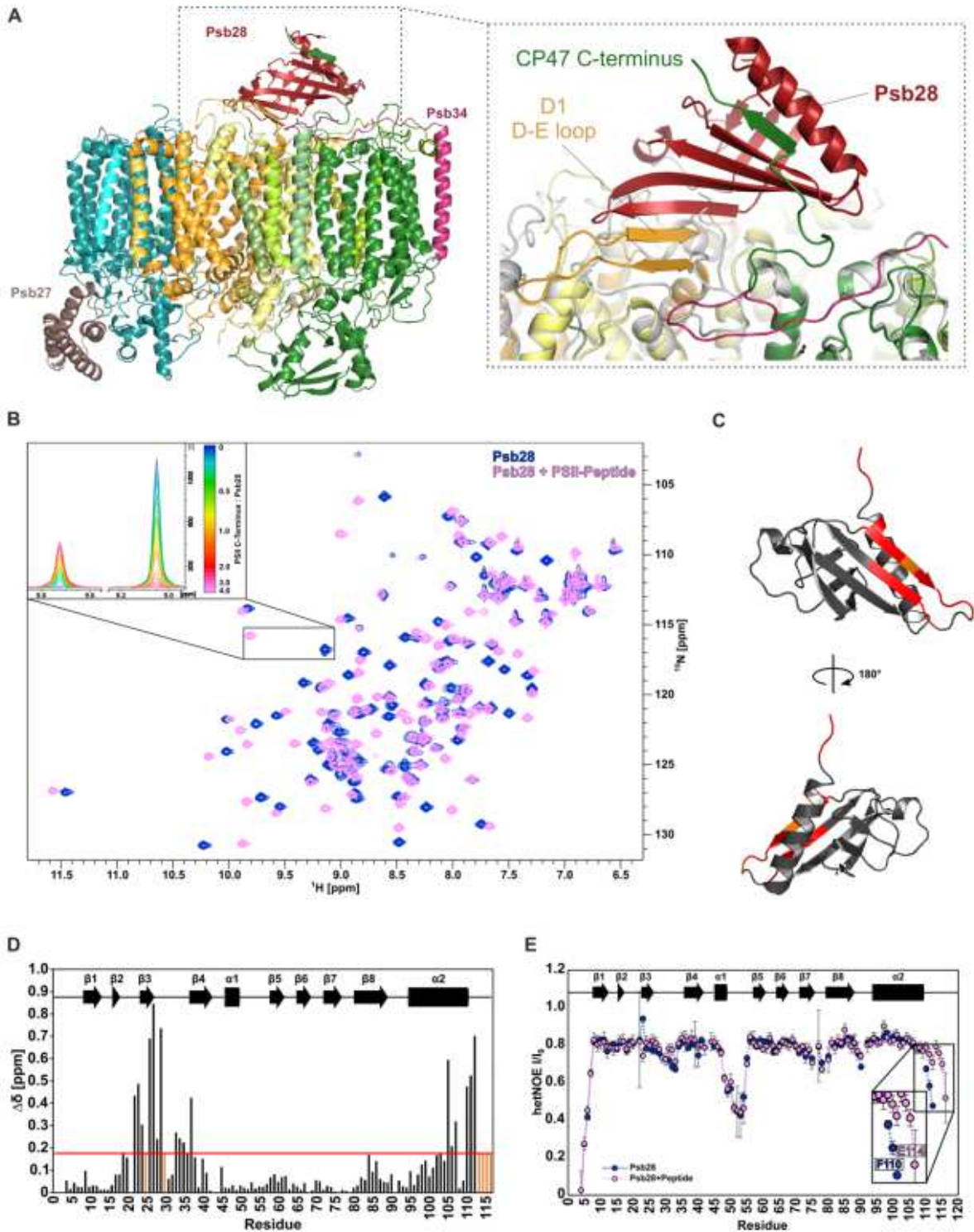


Figure 3

: The role of the CP47 C-terminus in binding of Psb28. (A). Binding of Psb28 at the cytoplasmic/stromal PSII surface (side view, colors correspond to Fig. 1) and continuation of the central Psb28 beta-sheet by the CP47 C-terminus and the D-E loop of D1 (dashed box). For comparison, mature monomeric PSII (PDB-

ID 3KZI) is shown in gray. (B) Superimposed 2D ^1H - ^{15}N -HSQC spectra of free Psb28 (blue) and Psb28 bound to the C-terminal peptide of CP47 (magenta). Upper left inset: representation of slow exchange behavior for the proton amide resonance of T24, ranging from 126.9 ppm to 128.6 ppm in the ^{15}N dimension. (C) CSPs of more than one SD projected onto the model representation of Psb28. (D) Weighted $^1\text{H}/^{15}\text{N}$ chemical shift perturbations observed for Psb28 upon binding to the CP47 peptide. Red line indicates one standard deviation (SD), residues that yield resonances only in the complex form are indicated in orange. (E) Backbone ^{15}N $\{^1\text{H}\}$ -heteronuclear NOE of free Psb28 (blue) and Psb28 bound to the C-terminal region of the CP47 peptide (magenta). Smaller I/I₀ ratios correspond to regions that exhibit dynamics on the pico- to nanosecond timescale.

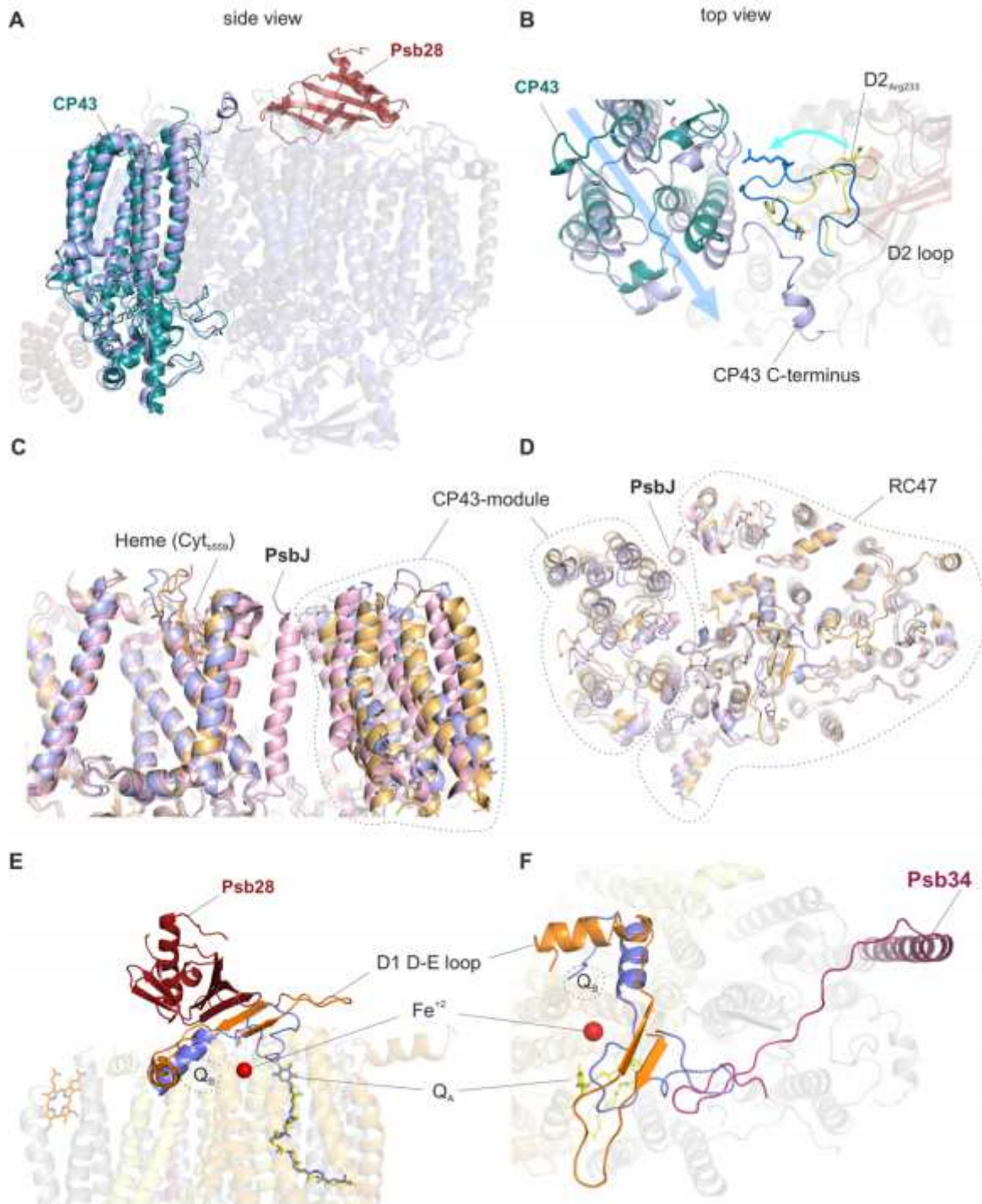


Figure 4

Structural changes of the D1 and D2 D-E loops induced by binding of Psb28 and Psb34. (A) Side view of the CP43 antenna protein in PSII-I (teal) and the PSII-M control (light blue). (B) Structural changes between PSII-I and the PSII-M control in the cytoplasmic D2 D-E loop (yellow: PSII-I, blue: PSII-M) and attachment of CP43 (teal: PSII-I, light blue: PSII-M control) (top view). Details of the structural changes in the D2 loop are shown in Fig. S5A and B. (C) Side view and (D) top view of the PSII-I structure (orange) compared to the PSII-M control (light blue) and mature monomeric PSII (light red, PDB-ID 3KZI). (E) Side view and (F) top view of the Psb28-induced structural changes in the D1 D-E loop (orange) and perturbation of the QB binding site compared to PSII-M (light blue), which lacks the assembly factors. QA is shown in yellow (PSII-I) or light blue (PSII-M), respectively. See Fig. S5C-H for enlarged views of the QA and QB binding site and the adjacent nonheme iron.

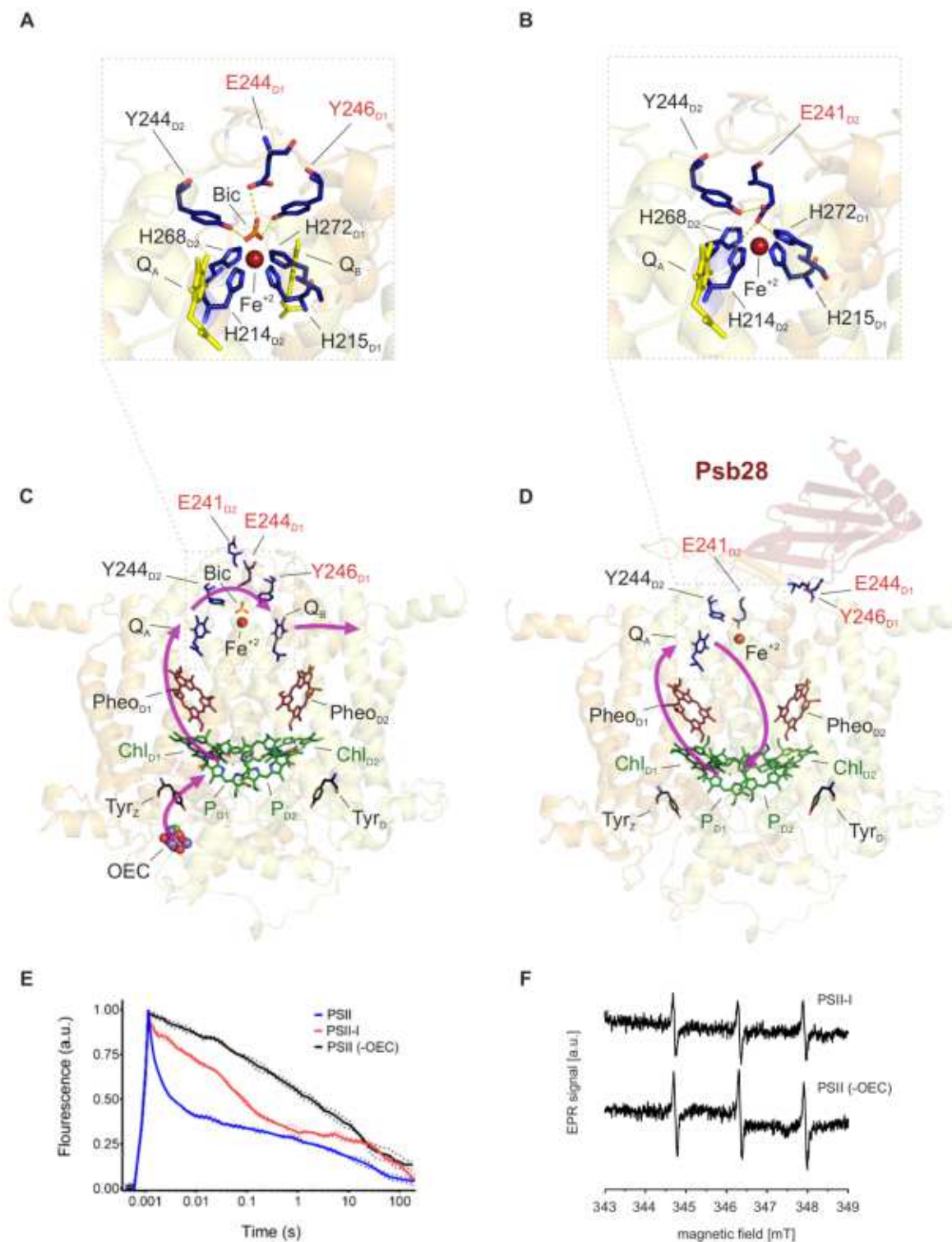


Figure 5

Binding of Psb28 displaces bicarbonate as a ligand of the non-heme iron and protects PSII from damage. (A) The electron transfer from PQA to PQB is coordinated by the non-heme iron (Fe^{2+}), with the binding of bicarbonate (Bic) serving as a regulatory mechanism⁴⁹ in mature PSII (PDB-ID 3WU2). (B) Binding of Psb28 to the PSII-H assembly intermediate induces a conformational change in the cytoplasmic D2 D-E loop, where the side chain of Glu241 replaces bicarbonate as a ligand of the non-heme iron. The

respective fits of the non-heme iron binding sites are shown in Fig. S5E and F. A similar coordination is also found in non-oxygenic bacterial reaction centers⁵³ (Fig. S6C). (C) Electron transfer (purple arrows) in mature PSII. Light-induced charge separation at the reaction center chlorophylls (PD1, PD2, ChlD1, ChlD2) leads to electron transfer via pheophytin (PheoD1) and plastoquinone A (QA) towards QB. The electron gap at the reaction center is filled by the oxygen evolving complex (OEC). (D) Reoxidation of QA⁻ by direct and safe charge recombination is favored in the PSII assembly intermediate, as indicated by the purple arrows. (E) Flash-induced fluorescence decay of PSII. Blue lines represent active PSII, black and red represent PSII without functional OEC and PSII-I respectively. Dotted corridors depict SD (n = 3). (F) The protective role of Psb28 binding was further confirmed by EPR spectroscopy using the spin probe TEMPD, which is specific for 1O_2 , the major reactive oxygen species in PSII generated by triplet chlorophyll (3 P). Inactivated PSII without functional Mn₄CaO₅ cluster (-OEC) was used as control.

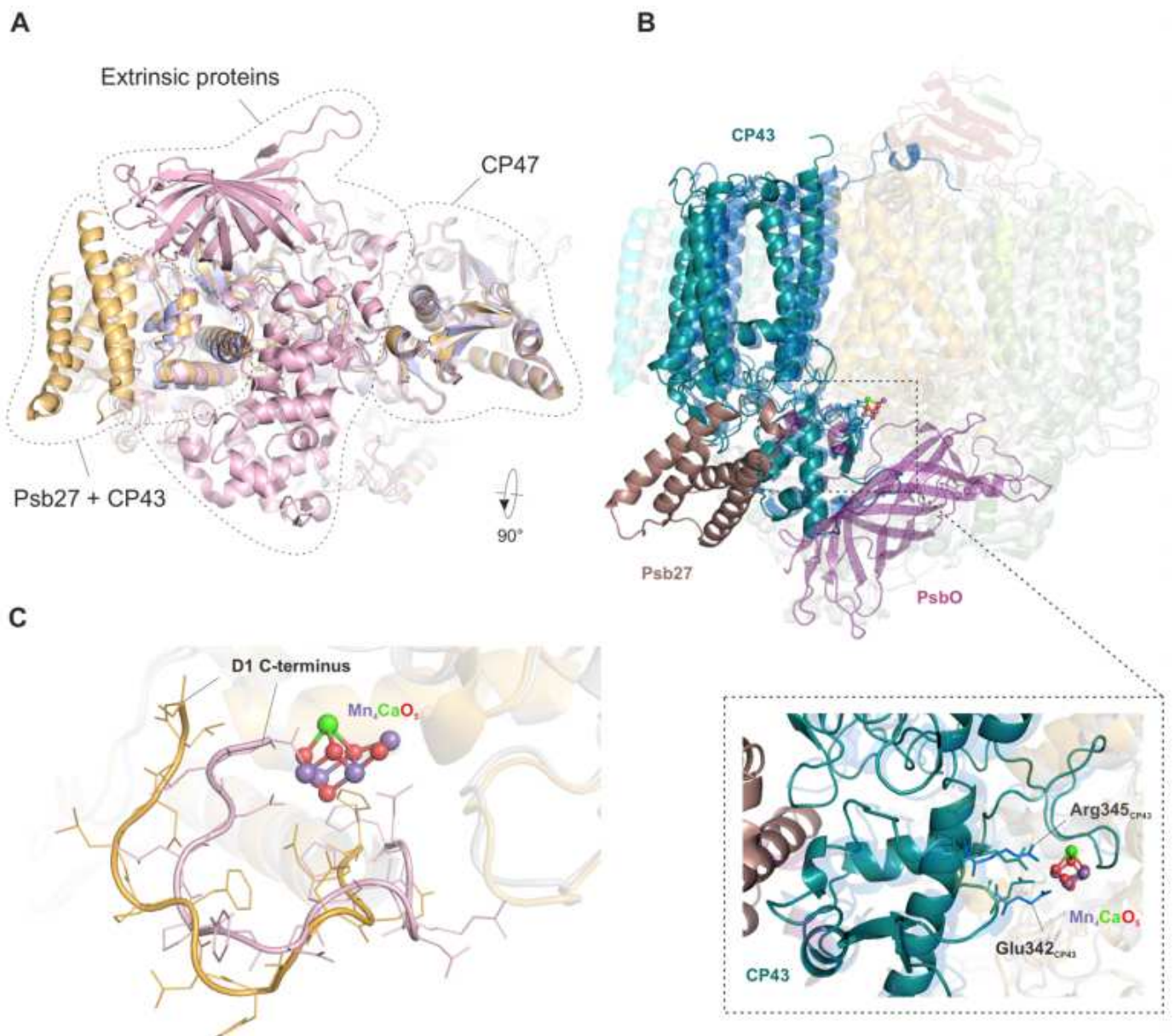


Figure 6

The role of Psb27 in Mn₄CaO₅ cluster assembly. (A) Bottom view of the luminal PSII surface for PSIII (orange), the PSII-M control (light blue) and mature monomeric PSII (PDB-ID 3KZI) (light red). (B) Side view of CP43 (teal) and Psb27 (brown) in PSII-I, as well as of CP43 (blue) and PsbO (purple) in mature monomeric PSII (PDB-ID 3KZI). Dashed box: CP43 E loop with residues Arg345 and Glu342 (shown as sticks), which are involved in coordination of the Mn₄CaO₅ cluster. We changed the numbering of CP43 residues due to a corrected N-terminal sequence (www.UniProt.org). The residues correspond to Arg357 and Glu354 in previous publications. The high-resolution structure of the Mn₄CaO₅ cluster is taken from Umena et al. 2011 (PDB-ID 3WU2). (C) Position of the D1 C-terminus in PSII-I (orange) and mature monomeric PSII (PDB-ID 3KZI) (light red).

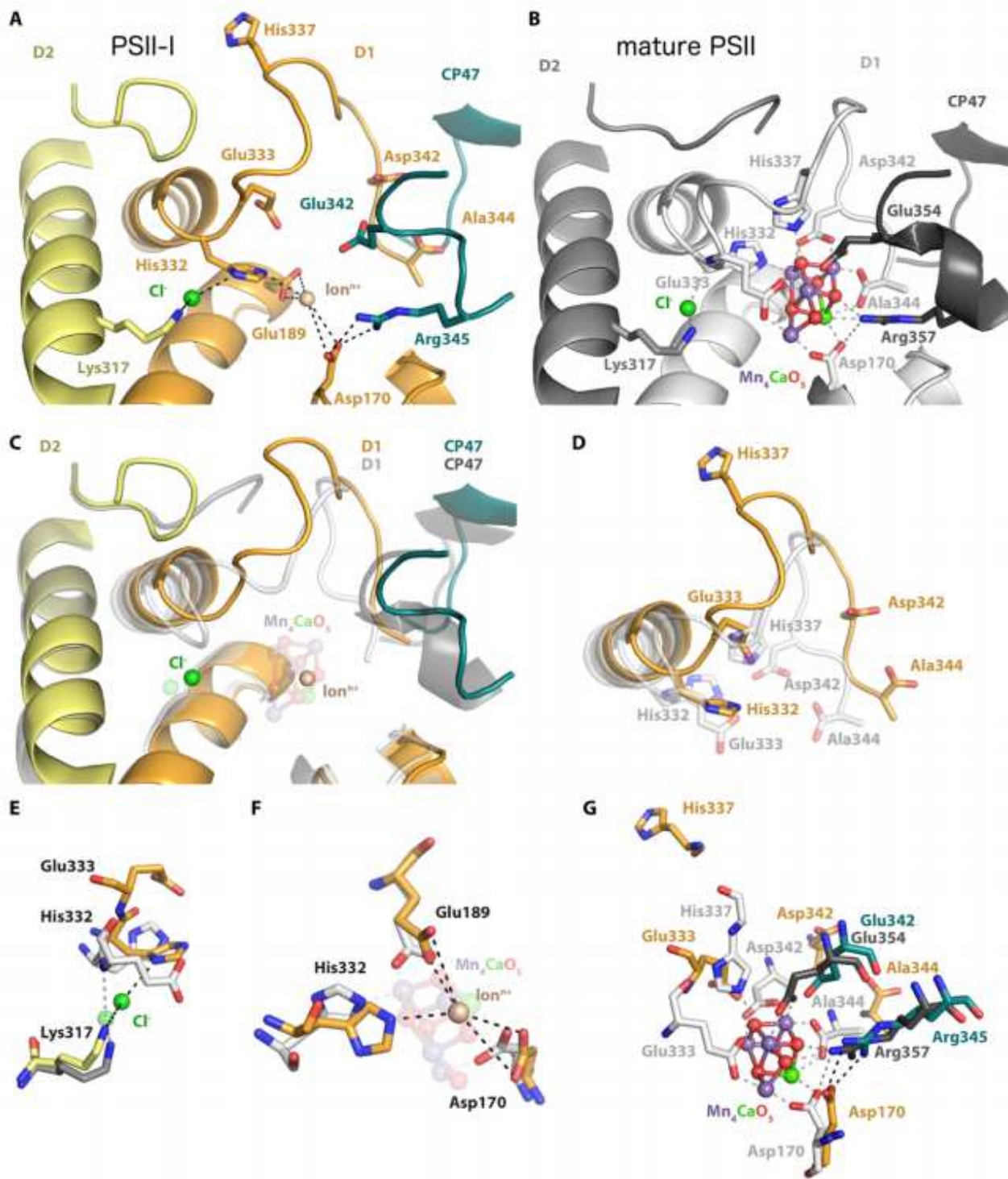


Figure 7

Conformational changes within the active site of the Mn₄CaO₅ cluster. The Mn₄CaO₅ cluster performs PSII's unique water-splitting reaction. (A) The active site of the Mn₄CaO₅ cluster is resolved within our PSII-I structural model but is not yet oxygen-evolving. (B) Crystal structure of the oxygen-evolving, mature PSII (PDB-ID 3WU2, resolution 1.9 Å). (C) Overlay of both structures, illustrating significant differences in the backbone conformation of the D1 and D2 C-terminal tails. (D) Accompanying side chain

rearrangements of the D1 C-terminus. The Cl⁻ (E), Ion⁺ (F) and Mn₄CaO₅ (G) cluster coordination partners are compared in detailed. The validation of the fit to density for the structural details shown here is provided in Figure S7.

Supplementary Files

This is a list of supplementary files associated with this preprint. Click to download.

- [SupMovie1.mp4](#)
- [03NaturePlantsSupplementary01withref.pdf](#)
- [SupMovie2.mp4](#)
- [SupMovie3.mp4](#)
- [SupMovie4.mp4](#)